Public Interest Energy Research (PIER) Program
FINAL PROJECT REPORT

GEOTHERMAL EXPLORATION IN EASTERN CALIFORNIA USING ASTER THERMAL INFRARED DATA

Prepared for: California Energy Commission
Prepared by: Imageair, Inc.

Imageair, Inc.

APRIL 2010
CEC-500-2012-005

Prepared by:

Primary Author:
Mariana Eneva

Imageair, Inc.
San Diego, California 92126

Contract Number: PIR-04-006

Prepared for:

California Energy Commission

Pablo Gutierrez
Project Manager

Linda Spiegel
Office Manager
Energy Generation Research Office

Laurie ten Hope
Deputy Director
RESEARCH AND DEVELOPMENT DIVISION

Robert P. Oglesby
Executive Director

DISCLAIMER

This report was prepared as the result of work sponsored by the California Energy Commission. It does not necessarily represent the views of the Energy Commission, its employees or the State of California. The Energy Commission, the State of California, its employees, contractors and subcontractors make no warrant, express or implied, and assume no legal liability for the information in this report; nor does any party represent that the uses of this information will not infringe upon privately owned rights. This report has not been approved or disapproved by the California Energy Commission nor has the California Energy Commission passed upon the accuracy or adequacy of the information in this report.

Acknowledgements

This project greatly benefited from the participation of the following individuals and organizations:

Geothermal Program Office/U.S. Navy, China Lake, CA - Frank Monastero (a former head of GPO) made it possible to collect field data at the Coso geothermal field during two field trips in the summer of 2006. Many labor hours were contributed by GPO staff, representing the equivalent of a significant financial contribution to the project, at no cost to the California Energy Commission. In particular, Steve Bjornstad helped significantly with installing and monitoring temperature probes, accompanying the PI in the field, and spending time for extensive discussions. Chris Page and Dave Meade also helped with the field trips.

Xiaoliang Wu (Department of Mathematics, Informatics, and Statistics, Commonwealth Scientific and Industrial Research Organization – CSIRO, Australia) – performs orthorectification of ASTER scenes, at no cost to the Commission.

Mark Coolbaugh (Great Basin Center for Geothermal Energy, University of Nevada Reno) – helped with choosing the ASTER scenes for analysis, determination of ground control points (GCP) that are being used by Dr. Wu in the orthorectification, identifying the best procedures for the data analysis, and planning and execution of field trips in eastern California to measure temperatures with 2-m probes (May- June 2009).

Chris Kratt (Desert Research Institute, Nevada, Reno) – performed measurements with 2-m temperature probes during field trips in eastern California (May-June 2009).

Bhaskar Ramachandran (Land Processes Distributed Active Archive Center (LPDAAC)/ U.S. Geological Survey, Sioux Falls, SD) – helped with acquiring numerous ASTER scenes. He invested time and efforts at no cost to the Commission.

ASTER team – current and former members provided help to the PI in connection to the obtaining and the analysis of ASTER data, and a field trip to Coso in July 2006. In particular, the U.S. Science Team Leader, Michael Abrams from the Jet Propulsion Laboratory (JPL), allowed the use of resources at no cost to the Commission. Leon Maldonado (JPL) helped with Data Acquisition Requests (DAR) to collect ASTER data over eastern California, particularly nighttime scenes that were relatively lacking, and daytime-nighttime pairs that are very rare unless specifically scheduled. Elsa Abbott (JPL) helped with radiosonde measurements during a July 2006 field trip to Coso. Hideyuki Tonooka from the Department of Computer and Information Sciences, Ibaraki University (Japan) and Andrew French from the U.S. Department of Agriculture helped with discussions on the use of the ASTER thermal infrared (TIR) data and ran their algorithms on some sample scenes.

Jim Combs – helped with the organization of and measurements during a July 2006 field trip to the Coso geothermal field.

Doug Stow and Pete Coulter (Geography Department, San Diego State University - SDSU) - provided an ASD FieldSpec spectroradiometer for reflection measurements during field trips to the Coso geothermal field in the summer of 2006.

Please cite this report as follows:

Eneva, M. 2010. *Geothermal Exploration in Eastern California Using ASTER Thermal Infrared Data*, California Energy Commission, PIER Program, CEC-500-2012-005.

Preface

The California Energy Commission's Public Interest Energy Research (PIER) Program supports public interest energy research and development that will help improve the quality of life in California by bringing environmentally safe, affordable, and reliable energy services and products to the marketplace.

The PIER Program conducts public interest research, development, and demonstration (RD&D) projects to benefit California.

The PIER Program strives to conduct the most promising public interest energy research by partnering with RD&D entities, including individuals, businesses, utilities, and public or private research institutions.

PIER funding efforts are focused on the following RD&D program areas:

- Buildings End-Use Energy Efficiency
- Energy Innovations Small Grants
- Energy-Related Environmental Research
- Energy Systems Integration
- Environmentally Preferred Advanced Generation
- Industrial/Agricultural/Water End-Use Energy Efficiency
- Renewable Energy Technologies
- Transportation

Geothermal Exploration in Eastern California Using ASTER Thermal Infrared Data is the final report for the PIER project (grant number PIR-04-006) conducted by Imageair Inc. The information from this project contributes to PIER's Renewable Energy Technologies Program.

For more information about the PIER Program, please visit the Energy Commission's website at www.energy.ca.gov/research/ or contact the Energy Commission at 916-327-1551.

Table of Contents

Abstract ix
Executive Summary 1
1.0 Introduction 5
2.0. Project Methods 9
2.1. Data 9
2.2 Removal of Artifacts 10
2.2.1 Effect of Topographic Slope Aspect 10
2.2.2. Effect of Albedo 11
2.2.3. Effect of Thermal Inertia 11
2.2.4. Methodology to Correct for Slope Aspect, Albedo and Thermal Inertia 11
2.2.5. Effect of Elevation and Thermal Inversions 14
2.3. Orthorectification 15
2.4. Field Trips 16
3.0 Project Results 17
3.1. Choice of ASTER Data 17
3.2. Orthorectification 18
3.3. Imagery Corrections 20
3.4. Effects of Elevation and Temperature Inversions 27
3.5. Field Trips 32
3.5.1. July 2006 32
3.5.2. August 2006 35
3.5.3. May and June 2009 38
4.0 Conclusions and Recommendations 47
5.0 References 48

List of Figures

Figure 1-1. Map of geothermal resources in eastern California. 5
Figure 1-2. Study region shown on Google Earth image 6
Figure 1-3. Coso geothermal field within the boundaries of the Naval Air Weapons Station, China Lake, California. 7
Figure 1-4. Mineral alteration and hot surface features at the Coso geothermal field, California 7
Figure 1-5. Tufa formations at Mono Lake, California 7
Figure 1-6. Mineral alteration near Hot Creek, California 8
Figure 2-1. Effect of topographic slope aspect on a daytime thermal image. 10

Figure 2-2. Albedo effect. 12
Figure 2-3. Thermal inertia effect. 13
Figure 3-1. Spatial coverage from the bets available daytime/nighttime ASTER image pairs. 18
Figure 3-2. Topographic variability in the Coso Geothermal area. 19
Figure 3-3. Level 1B TIR band 14, daytime (08/24/2001) and nighttime (08/22/2001). 20
Figure 3-4. Daytime AST_08 collected over the Coso geothermal field in August 2006. 21
Figure 3-5. Nighttime AST_08 collected over the Coso geothermal field in August 2006. 21
Figure 3-6. Example of changes in solar irradiation in the course of a day, depending on the topographic slope aspect. 22
Figure 3-7. Comparison of the uncorrected nighttime AST_08 with the corrected one, from the overlapping area of the image pair shown in Fig. 3-3. 23
Figure 3-8. Level 1B VNIR radiance in RGB (red-green-blue) for the area of overlap between the daytime and nighttime TIR scenes from Fig. 3-3. 23
Figure 3-9. Comparison of the nighttime uncorrected and corrected AST_08 images (surface temperature) for the same five areas (here outlines with white) in the Coso geothermal field, marked in Fig. 3-8. 24
Figure 3-10. Corrected AST_08 (surface temperature) in the overlapping area of the day-time/nighttime pair from August 2006. 25
Figure 3-11. Vegetation index, NDVI = (band3-band2)/(band3+band2), for the Coso area. 26
Figure 3-12. ASTER Level 1B VNIR (shown in RGB) from the Mammoth area. 26
Figure 3-13. Nighttime AST_08 (surface temperature) images over inset from Fig. 3-12. 27
Figure 3-14. Nighttime density plot of surface temperature versus elevation extracted from a nighttime AST_08 image collected over Coso in August 2006. 28
Figure 3-15. Daytime density plot of surface temperature versus elevation extracted from a daytime AST_08 image covering the same area as in Fig.3-14. 29
Figure 3-16. Map representation of the nighttime temperature inversions. 30
Figure 3-17. Examples of nighttime temperature inversions from ASTER TIR imagery. 31
Figure 3-18. Subsurface temperatures measured at 13 locations (blue circles in map insets) across hydrothermal features, as indicated. 33
Figure 3-19. Thermal images taken in the field during the night with a FLIR-P65 infrared camera. 35
Figure 3-20. Surface temperature measured with a hand-held FLIR-P65 infrared camera close to the times of satellite passages. 35
Figure 3-21. Launching a radiosonde for atmospheric measurements. 35
Figure 3-22. ASTER coverage of the Coso KGRA extracted from two Level 1B VNIR images collected on August 22, 2006. 36
Figure 3-23. Examples of reflec-tion spectra collected in the field with an ASD FieldSpec spectroradiometer. 37
Figure 3-24. Reflectance measured at various locations with a hand-held ASD FieldSpec spectroradiometer. 37
Figure 3-25. Surface temperature measurements with an infrared thermometer over two days in August 2006. 38
Figure 3-26. Deploying of 2-temperature probes. 39
Figure 3-27. Shaded relief image showing location of areas where 2-m temperature probes were deployed. 40

Figure 3-28. Measurements of 2-m temperatures. 42
Figure 3-29. Example of a pattern of shallow temperature measurements delineating a geothermal anomaly. 44
Figure 3-30. Example from Owens Valley, where lower albedo causes greater absorption of solar energy and therefore warmer 2-meter background tempera-tures. 46
Figure 3-31. Example from Fremont Valley, where data significantly below the albedo-temperature background line are associated with shallow groundwater in the valley bottom near irrigated fields. 46
Figure 3-32. 2-meter temperatures and associated albedos from the Columbus Marsh playa, Nevada. 46

List of Tables

Table 3-1. A list of best ASTER image pairs for the study region 17
Table 3-2. Examples of residuals and RMS from orthorectification 19

Abstract

Remote sensing is a cost-effective tool that can be used to cover large areas for the purpose of geothermal exploration. A particular application is the use of satellite thermal infrared (TIR) imagery from the Advanced Spaceborne Thermal Emission and Reflection Radiometer (ASTER) instrument aboard an orbiting satellite. It can be used to search remotely for elevated surface temperatures, which may be associated with geothermal resources. The study region is in the central part of eastern California, with emphasis on the Coso geothermal field. Nighttime scenes are most useful, because of the significantly diminished effect of solar irradiation compared with daytime. However, daytime scenes are also used for correction purposes. It is shown that TIR imagery cannot be interpreted correctly without proper removal of various effects that are not related to geothermal characteristics. These effects are caused by factors such as terrain distortion due to topographic variability, topographic slope aspect (southern slopes are warmer than northern slopes), albedo (dark-colored surfaces are warmer than light-colored ones), thermal inertia (surfaces with low thermal inertia cool off more at night), elevation (areas at lower altitudes are warmer than those at higher altitudes), and temperature inversions (local meteorological conditions sometimes cause cooler temperatures at the bottom of valleys and warmer temperatures higher up). Taking these effects into account makes it possible to reveal temperature anomalies, which are otherwise not distinguishable in the uncorrected imagery. Ground-based measurements were also carried out during several field trips, some of which took place concurrently with the satellite passages and ASTER data collection. The integration of remote sensing with field observations is promising for future exploration studies.

Keywords: Remote sensing, thermal infrared, TIR, ASTER, temperature anomalies, thermal anomalies, geothermal, Coso, eastern California

Executive Summary

Introduction

Remote sensing represents observations from airplanes and satellites carrying instruments on board that measure properties of the Earth' surface. Measurements can be done with different wavelengths, such as optical and thermal infrared remote sensing can be used to determine surface temperature. The best current satellite instrument for thermal infrared measurements is the Advanced Spaceborne Thermal Emission and Reflection Radiometer, a Japanese instrument mounted on the United States satellite Terra. There exists an archive of previously collected Advanced Spaceborne Thermal Emission and Reflection Radiometer data, as well as it is possible to order future data over chosen areas and time periods.

Purpose

Remote sensing is a promising tool in geothermal exploration for the purpose of a cost-effective evaluation of the Earth's surface properties over large areas. If markers of geothermal resources are detected with remote sensing, it is then possible to zero-in on prospective smaller areas for more expensive and targeted ground-based studies.

Project Objectives

The objective of this project was to use Advanced Spaceborne Thermal Emission and Reflection Radiometer thermal infrared data to search for anomalies in surface temperatures that may be associated with geothermal resources in the central part of eastern California. This is valuable in view of the increasing role of renewable energy, including that from geothermal energy.

Project Outcomes

The project was focused on eastern California, with emphasis on the Coso geothermal field. The major outcome is the detailed understanding of the factors influencing satellite thermal infrared imagery, so that true temperature anomalies are distinguished from anomalies unrelated to geothermal activity. Without filtering out the effects of these factors, the thermal infrared imagery would remain an incomprehensible mixture of warmer and cooler areas not necessarily related to real subsurface features.

Most useful is nighttime thermal infrared imagery, because it is less affected by the solar irradiation during the day. However, daytime thermal infrared and optical reflection imagery is also used in order to take into account effects that last into the night, even though they are strongest during the day. In this connection, daytime/nighttime pairs of thermal infrared scenes collected 12 hours and 36 hours apart are utilized. In addition to existing pairs of this type, additional Advanced Spaceborne Thermal Emission and Reflection Radiometer pairs were specifically ordered to be acquired during several satellite passages.

Factors identified and described in detail include the effects of:

- terrain distortion - when topography in the study area spans a large range of elevations, it is difficult to know the exact geographic position of the individual pixels in the satellite imagery and the results are skewed; hence a geometrical correction is needed. This will correct the aerial photographs so that it is uniform and can be measured on a map.
- topographic slope aspect - southern slopes are warmer than northern slopes;
- albedo - surfaces with lighter color reflect more of the solar irradiation and thus remain cooler than darker surface;
- thermal inertia - surfaces with lower thermal inertia cool off faster from the day into the night;
- elevation - surface temperatures are generally lower at higher altitudes; and
- temperature inversions - local meteorological conditions with a reverse elevation effect, i.e. with lower temperatures at lower altitudes, mostly observed at night.

None of the above effects are related to subsurface geothermal activity and they have to be filtered out. It is demonstrated, that after certain corrections, surface temperature anomalies can be identified that are otherwise not seen in the uncorrected thermal infrared imagery.

In addition, field trips were conducted, during which ground-based measurements were collected. Some of these field experiments were specifically planned to be concurrent with the passage of the Terra satellite and collection of Advanced Spaceborne Thermal Emission and Reflection Radiometer thermal infrared daytime and nighttime imagery at the same time as field measurements were taken. The ground-based measurements included the use of temperatures probes at 1-meter and 2-meter depths, infrared camera, infrared thermometer, and spectral radiometer. Some of the measurements were limited to the Coso geothermal field, while the 2-meter temperature measurements were carried out in eight different valleys in eastern California.

Conclusions

Satellite thermal infrared imagery can be potentially very useful in outlining surface temperature anomalies possibly associated with geothermal resources. However, the TIR imagery can be only used after appropriate corrections, so that only surface features associated with subsurface properties of geothermal resources are identified, and unrelated factors are filtered out.

Recommendations

- Orthorectification - The major issue to be resolved in future similar studies is the current inadequacy of these geometric correction methods. It will be important to assure easily accessible geometric correction techniques that can successfully work with the satellite thermal infrared products from Advanced Spaceborne Thermal Emission and Reflection Radiometer and successor satellite sensors. Only then will it be possible to tackle at once large areas with significant topographic variability, rather than laboriously analyzing individual small and relatively flat areas. Once the proper geometric correction is assured, it is recommended that more areas are studied using the methodology described in this report.

- Search for unknown geothermal resources – After temperature anomalies are unambiguously identified in known geothermal areas, it is recommended to look for similar markers in other areas that may be prospective future sites of geothermal production.

- Mineral alteration – In the future it will be important to enlarge the scope of the satellite thermal infrared studies and use remote sensing data to also search for signs of mineral alteration associated with geothermal resources. This would assure a more complete utilization of the available remote sensing data and capabilities, which will augment the search for temperature anomalies described in the report.

Benefits to California

The immediate benefit to California is that a prospective region of geothermal resources began to be examined for temperature anomalies and possible pitfalls in such studies were clearly identified. This would significantly facilitate future exploration studies of this type, because it has been already established how to distinguish between real and irrelevant temperature anomalies in satellite thermal infrared imagery.

The long-term benefit to California is that such methods, in conjunction with other applications of remote sensing, may contribute to the discovery of new geothermal resources. These new geothermal resources, in turn, will be important for the future increase of the proportion of renewable energy used in electricity generation, which is in line with the energy planning on a state level. Opening of new geothermal plans will also contribute to creating new jobs in the state.

1.0 Introduction

Remote sensing data can be used as a cost-effective tool to explore large areas for geothermal potential and pinpoint smaller target areas for further exploration using more expensive airborne or ground-based surveys. Recent advances in thermal infrared (TIR) remote sensing open new opportunities for geothermal exploration. This project focuses on the use of satellite imagery collected by the Advanced Spaceborne Thermal Emission and Reflection Radiometer (ASTER), mounted on the Terra satellite. The study region (Figures 1-1 and 1-2) is between the Coso Geothermal Power Project (Figures 1-3 and 1-4) and the Mammoth Geothermal Power Project, both located in the central part of eastern California. This region is suspected to have significant geothermal resources. For example, there is evidence of geothermal activity, such as tufa columns (Figure 1-5) and mineral alteration (Figures 1-4 and 1-6). However, due to the lack of access infrastructure, there has been little geothermal exploration conducted in the region. The purpose of the project was to identify the thermal signatures of known geothermal sites and subsequently search for similar features in unexplored areas.

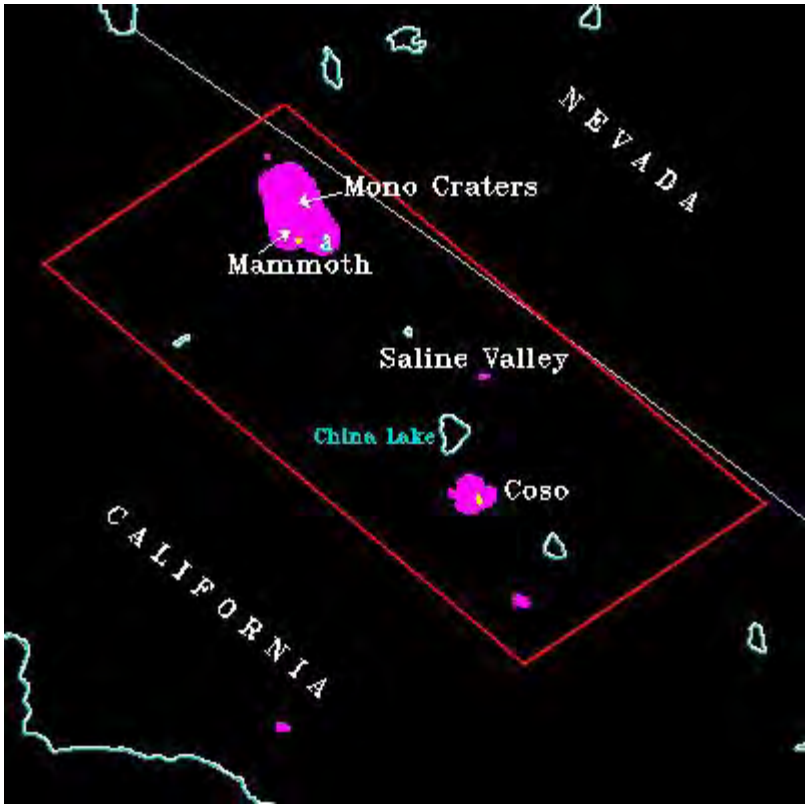

Figure 1-1. Map of geothermal resources in eastern California. Known geothermal resources areas (KGRAs) are shown in pink. Two production areas (in Coso and Mammoth) are shown in yellow in the midst of the KGRAs. Polygon outlined in red is study region.

All this is important in view of the increasing interest in electricity generation from renewable resources and, in particular, tapping into the potential 4,000 megawatts of additional power from geothermal energy in California (Sass and Priest 2002). Based on some projections, the U.S. will need to increase its current electrical power generating capacity by 40% (~300,000 MWe) over the next 15 years (Williams 2002). The U.S. Geological Survey has estimated that there is a potential for about 22,000 MWe of electrical power generation in the western U.S. from identified high-temperature (>150°C) geothermal systems at depths less than 3 km. Estimates of potential geothermal power production from undiscovered resources range between 72,000 and 127,000 MWe. Spaceborne remote sensing is particularly cost-effective in the search for new geothermal resources, as long as attributes associated with geothermal fields can be identified.

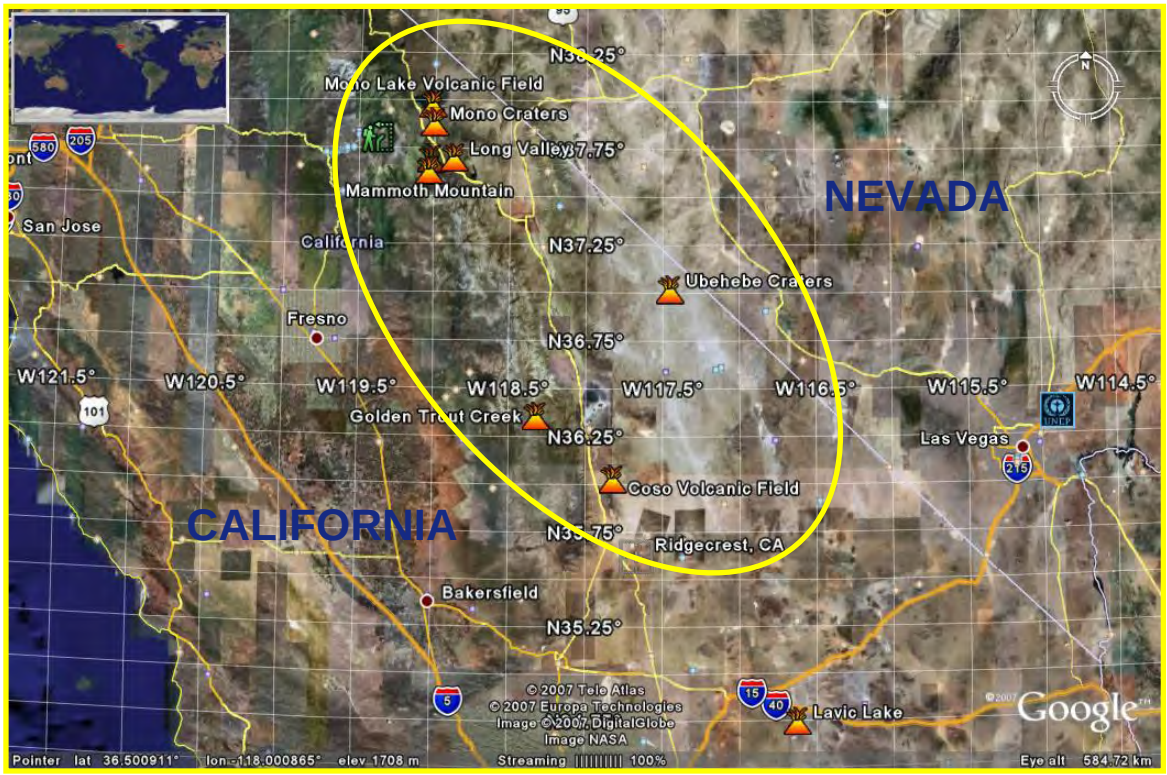

Figure 1-2. Study region shown on Google Earth image

Attributes to search for with TIR remote sensing would be related to high heat flow anomalies, excess vertical temperature gradients, and surface thermal manifestations. Some surface features above geothermal reservoirs are obviously hot, such as geysers, hot springs, fumaroles, and mud pools. Less obvious surface attributes of geothermal fields amenable to TIR remote sensing include locally elevated temperatures (e.g., Coolbaugh et al. 2007), geobotanical characteristics such as thermally stressed vegetation (e.g., Martini et al. 2000), bare altered ground, host rock permeability and topographic relief, and the presence of certain rock types and minerals (e.g., Kratt et al. 2006).

Previous applications of optical and infrared remote sensing to geothermal fields, both airborne and spaceborne, have sought to characterize the associated fracture systems and to capture specific surface expressions of the underlying geothermal reservoirs. Multispectral and hyperspectral *airborne* remote sensing has been long used over geothermal areas, including TIR scanning (e.g., Pickles et al. 2001; Allis et al. 1999; Coolbaugh et al. 2000; Martini et al. 2000). Earlier examples of *spaceborne* remote sensing include applications of data from Landsat TM, SPOT XS, and SPOT PAN imagery, at 30-m, 20-m, and 10-m spatial resolution (e.g., Cochrane et al. 1994). Calvin et al. (2002) used day/night ASTER scenes over the Brady Hot Springs geothermal area (Nevada), where they identified a thermal anomaly associated with a nearby fault. Corrections for topographic slope orientation, albedo, and thermal inertia (Coolbaugh et al. 2000; Coolbaugh 2003) have been shown to increase the number of remotely sensed thermal anomalies by an order of magnitude compared with remote sensing without such corrections. This type of work was continued as part of this project (Eneva et al. 2006, 2007; Eneva and Coolbaugh 2009) and still continues.

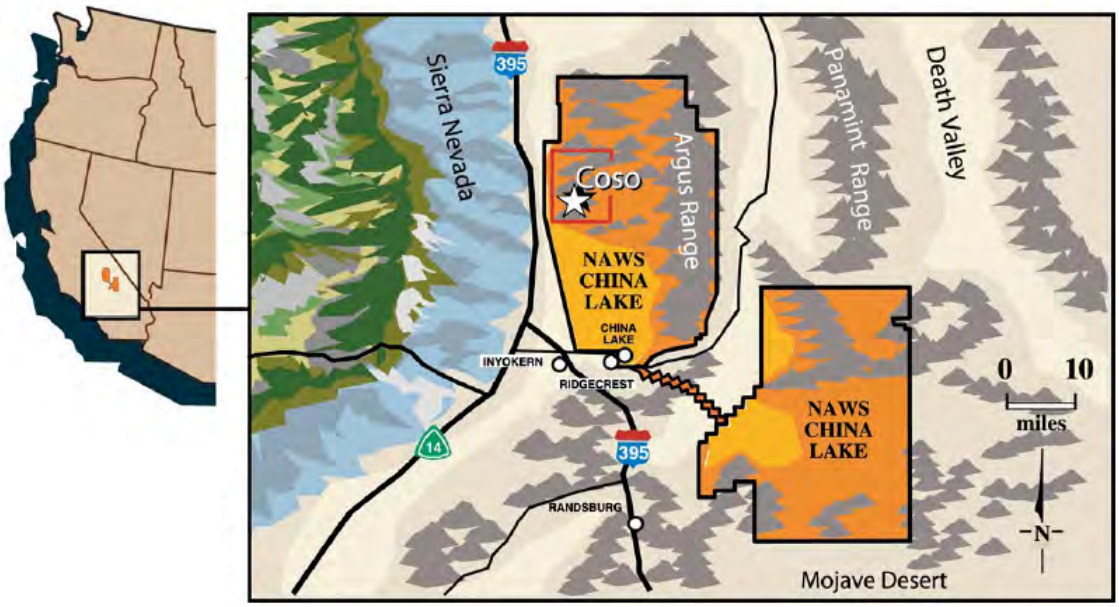

Figure 1-3. Coso geothermal field within the boundaries of the Naval Air Weapons Station, China Lake, California. From Monastero (2002).

Figure 1-4. Mineral alteration and hot surface features at the Coso geothermal field, California
Photo Credit: Mariana Eneva, Imageair Inc.

Figure 1-5. Tufa formations at Mono Lake, California

Photo Credit: Mariana Eneva, Imageair, Inc.

Figure 1-6. Mineral alteration near Hot Creek, California

Photo Credit: Mariana Eneva, Imageair Inc.

2.0. Project Methods

2.1. Data

The satellite data used in this project are from the Advanced Spaceborne Thermal Emission and Reflection Radiometer (ASTER) instrument (http://asterweb.jpl.nasa.gov/), with emphasis on the thermal infrared (TIR) band. It is a unique Japanese instrument mounted on the U.S. Terra satellite launched in December 1999. Compared with previous TIR remote sensing from satellites (e.g., Landsat, AVHRR), ASTER provides significantly more possibilities. Imagery is acquired over a 60-km wide swath; i.e., every scene covers an area of size ~60 km x 60 km. Multispectral images of the Earth's surface are provided in 14 different bands. The revisit time interval over any given site is 16 days, although data is not necessarily collected during every passage. It is possible to order data from the set of existing scenes in the archive, as well as to order future acquisitions. The ASTER channels are as follows: (1) three visible and near-infrared (VNIR) bands, with wavelengths between 0.5 μm and 0.9 μm, at 15-m spatial resolution; (2) six short-wave infrared (SWIR) bands 1.6 μm to 2.43 μm, at 30-m resolution; and (3) five thermal infrared (TIR) channels, 8 μm to 12 μm, at 90-m resolution. No other civilian satellite instrument provides TIR data in five bands.

Each ASTER scene can be ordered as several different products. Perhaps the most used ASTER data product is Level 1B (radiance at sensor). Higher-level data products are produced on demand and include surface radiance corrected for atmospheric effects – AST_09, reflectance – AST_07 and reflectance with cross-talk correction – AST_07XT, emissivity – AST_05, and surface kinetic temperature – AST_08. Temperature and emissivity could be calculated from Level 1B TIR as separate products (AST_08 and AST_05) only because ASTER has five TIR channels rather than only one. The so-called temperature-emissivity separation (TES) algorithm is used for this purpose (Gillespie et al. 1998). The primary products used in this project are AST_08 (temperature), and for correction purposes explained below, AST_07XT (reflection). All data were ordered from the EOS Data Gateway of the Land Processes Distributed Active Archive Center (LPDAAC). At present these same data can be ordered through the Warehouse Inventory Research Tool (WIST) - https://wist.echo.nasa.gov in the U.S. or through the Japanese ordering system, GDS (http://www.gds.aster.ersdac.or.jp).

The AST_07XT product (reflection) exists only for daytime scenes. However, AST_08 (temperature) can be produced for both daytime and nighttime scenes. In general, nighttime TIR is much more informative when searching for temperature anomalies, because the solar irradiation overwhelms daytime TIR. However, daytime TIR is useful to apply certain corrections, as explained below. In this project, of particular interest are daytime/nighttime pairs collected only 12 hours or 36 hours apart. Such pairs are rarely collected by chance and usually have to be ordered. Also, nighttime TIR in eastern California is frequently cloudy, so initially few of the nighttime images in the archive appeared useful. For this reason, more nighttime images and daytime/nighttime pairs were ordered, using so-called DAR (Data Acquisition Requests), which were facilitated through the help of staff at the Jet Propulsion Laboratory (JPL). As a result, the data archive now contains more nighttime images and

daytime/nighttime pairs collected over eastern California than would have been available without the efforts made for this project.

In addition to the satellite data, digital elevation model (DEM) data are used in this project for the purpose of orthorectification (see Section 2.3). These data are with 30-m spatial resolution and were ordered from the USGS (http://seamless.usgs.gov).

Finally, data were collected during several field trips. These included temperature measurements at 1-m and 2-m depths, as well as reflection measured on the surface to be used for albedo correction, as explained in Section 2.2.

2.2 Removal of Artifacts

2.2.1 Effect of Topographic Slope Aspect

Topography and albedo can have significant effect in a thermal image, because they influence the overall amount of energy available for heating. Topographic slope orientation is very important, with southern slopes receiving more of the flux of solar irradiance than the northern slopes. This effect is stronger in daytime thermal images, but endures at nighttime as well.

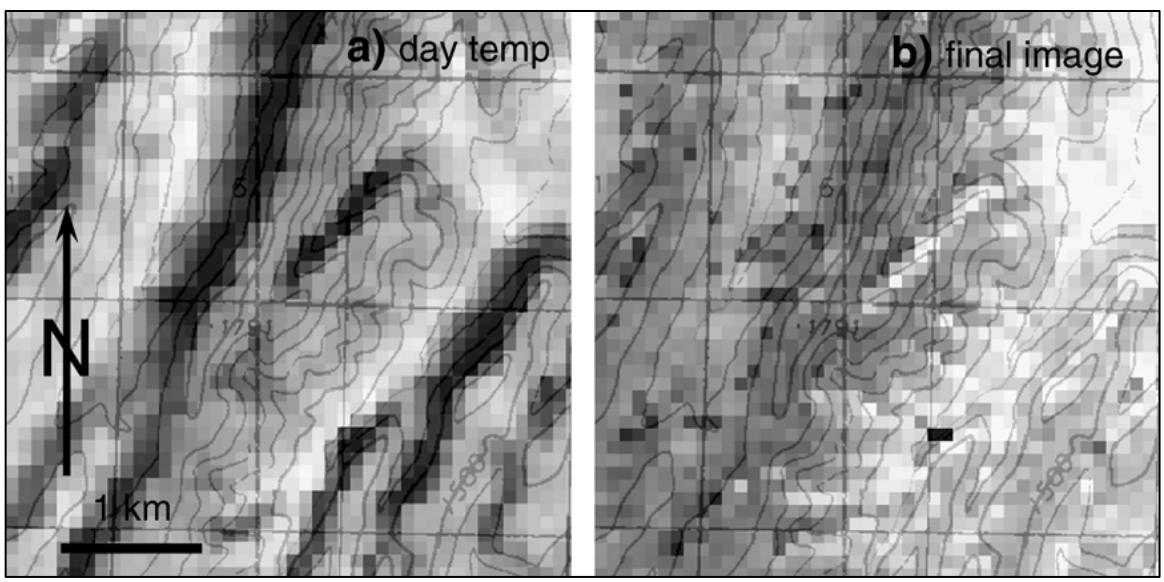

Figure 2-1. Effect of topographic slope aspect on a daytime thermal image. Brighter areas indicate higher surface temperatures. (a) Daytime temperature image AST_08; (b) processed image after corrections for albedo, topographic slope, and thermal inertia. Southeast-facing topographic slopes are warmer in the uncorrected image (a), but in the corrected image (b), residual temperatures are largely a function of elevation and not slope orientation. Example from Nevada, after Coolbaugh et al. (2007a).

Figure 2-1 illustrates this effect and shows results after correcting it. This effect translates into adjacent warmer and cooler areas in thermal remote sensing images. Figure 2-1a shows a daytime AST_08 image depicting surface temperature. This image illustrates a strong topographic slope aspect effect that can be removed (Fig. 2-1b) after suitable image processing described by Coolbaugh et al. (2007a) and applied in this project (Eneva et al. 2006, 2007).

2.2.2. Effect of Albedo

High albedo is related to higher reflectance and less energy remaining for heating, so light colored surfaces remain cooler compared with darker ones. Similar to the slope aspect effect, the albedo effect is stronger in daytime thermal images, but endures at nighttime as well. Figure 2-2 demonstrates this effect. Fig. 2-2a shows a Level 1B ASTER image from the VNIR (visible-near infrared) bands, where light surfaces indicate high albedo. Figs. 2-2b-d all show an AST_08 (surface temperature) image of the same area. The high-albedo areas are relatively cooler in both the daytime and nighttime AST_08 images, with weaker, but still noticeable effect at night. After appropriate corrections, the effect of albedo can be removed (Fig. 2-2d). Note that the only remaining dark (cool) spot in the upper right corner of the corrected image is due to vegetation and not to high albedo, hence it was not eliminated after the corrections.

2.2.3. Effect of Thermal Inertia

Thermal inertia indicates how fast a material gets heated and cools off. It is significantly affected by porosity. Lower values mean faster cooling off at night. Estimating thermal inertia can be a valuable tool to characterize material properties. However, here it is more important to remove the effect of thermal inertia in order to reveal or enhance thermal anomalies (e.g., when looking for geothermal resources). Thermal inertia can be approximately estimated from daytime/nighttime pairs of thermal satellite images – AST_08 in this project.

Figure 2-3 illustrates the effect of thermal inertia. Sand has high porosity, and hence, low thermal inertia. Thus it is relatively warm during the day (Fig. 2-3b), and relatively cool during the night (Fig. 2-3c). Note that both the daytime and nighttime AST_08 images (Figs. 2-3 b-c) are corrected for the effects of topographic slope/aspect and albedo, but the differences in thermal inertia are still obvious.

2.2.4. Methodology to Correct for Slope Aspect, Albedo and Thermal Inertia

Albedo and topographic slope aspect are treated together in terms of their influence on the overall amount of energy available for heating. A simplified heat energy model based on net surface radiation flux Q (Watson, 1973) is used as a basis to correct for albedo and topographic slope aspect (Coolbaugh, 2003; Coolbaugh et al., 2007a):

$$Q \sim (1-A)*M(Z)*\cos Z' , \qquad (1)$$

where Q is the net radiation flux at the surface, A is the ground albedo, cosZ′ is the cosine of the angle between the surface normal and the sun's rays (calculated as so-called *shaded relief*), Z is the zenith angle, and M(Z) is the atmospheric transmission depending on Z (Finlayson-Pitts and Pitts 1999). The shaded relief can be calculated from the sun's elevation and declination for any given date and time of a satellite passage. The albedo A can be obtained from:

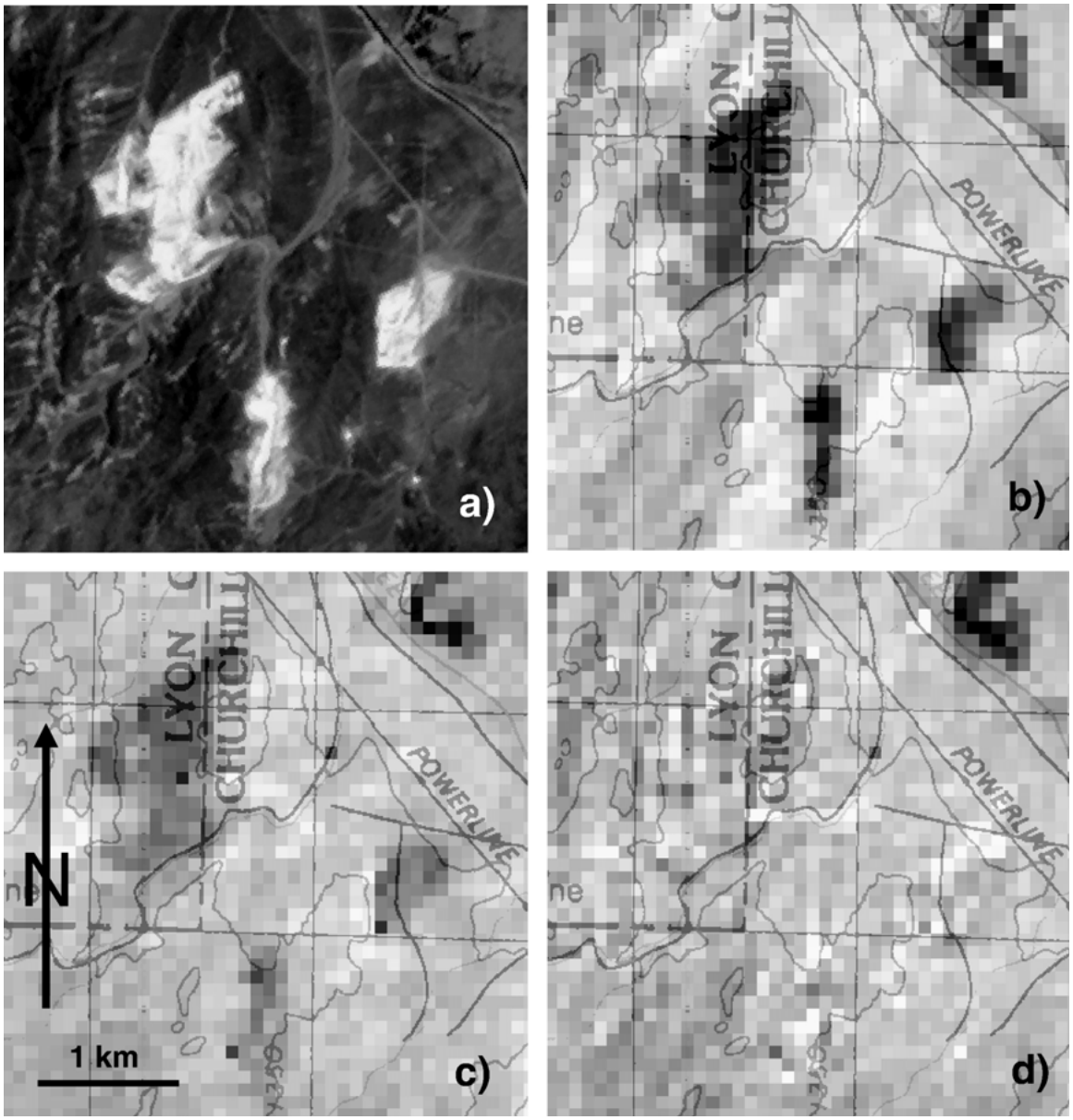

Figure 2-2. Albedo effect: (a) composite albedo image of ASTER bands 1, 2, and 3 (VNIR); (b) daytime temperature image AST_08; (c) nighttime temperature image; (d) final processed image after corrections for albedo, topographic slope, and thermal inertia. Highly reflective diatomite in three open pits appears cool in (b) and (c), but the temperature anomaly has been largely removed in the final processed image (d). In (b), (c), and (d), brighter areas indicate higher surface temperatures. The cooler area in the northeast corner of (b), (c), and (d) consists of grassy meadows. Example from Nevada, after Coolbaugh et al. (2007).

$$R_w = k_w * A_w * \cos Z' + b_w \quad , \qquad (2)$$

where R is taken from the AST_07XT product (surface reflectance) and cosZ′ is the shaded relief calculated for the moment of satellite passage. The three different VNIR bands are

marked with a w subscript. The final albedo estimate is the weighted average from the estimates in the three individual bands. The constants k_w and b_w can be estimated from field measurements (see Section 3.5.2), and would be 1 and 0, respectively, if the AST_07XT imagery were perfectly corrected for atmospheric absorption and scattering effects.

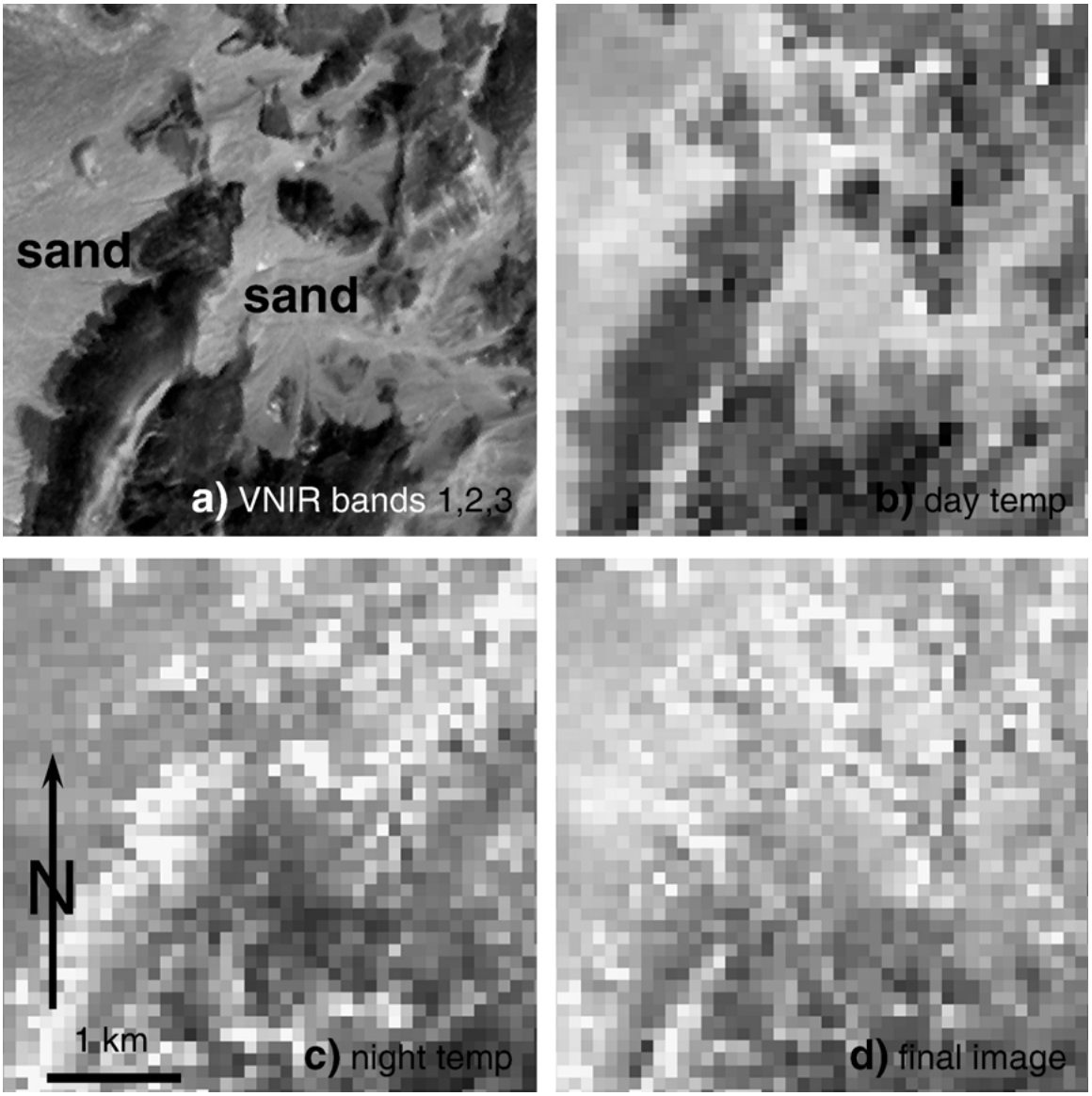

Figure 2-3. Thermal inertia effect: (a) composite image of ASTER bands 1, 2, and 3 (VNIR); (b) day temperature image AST_08 after corrections for albedo and topographic slope; (c) night temperature image after corrections for albedo and topographic slope; (d) final processed image after corrections for thermal inertia. Because of its lower thermal inertia, sand in valleys appears warm in the daytime image (b) relative to outcropping basalt, and appears relatively cool in the night image. After corrections for thermal inertia in the final enhanced image (d), temperatures appear warmer at lower elevations (meteorological effect). In (b), (c), and (d), brighter areas indicate higher surface temperatures. Example from Nevada, after Coolbaugh et al. (2007a).

The heat flux equation (1) is integrated over time to model changes in the intensity of light and the position of the sun relative to the topographic slopes over the course of a day:

$$E \sim (1-A)*\Sigma_t[M(Z)_t*\cos Z'_t*D_t]*\Delta t_t \quad , \qquad (3)$$

where E is the solar energy absorbed per unit area over the course of a day; Δt_t is the time interval for each component of the sum; D_t is a time decay factor ranging from 0 to 1, which is inversely proportional to the time gap between a given position of the sun and the time the imagery was acquired.

This simplified model accounts approximately for heat dissipation and can be used to calculate pseudo-temperature images to be subtracted from the AST_08 (surface temperature) daytime and nighttime images. Note that despite cooling off after sunset, the nighttime scenes would be still affected by differential heating from the previous day. This is especially true because the Terra satellite on which the ASTER instrument is mounted passes only several hours after sunset and not in the pre-dawn hours. Even pre-down data needed corrections in order to reveal a geothermal anomaly (Coolbaugh et al. 2007a).

The effect of thermal inertia can be accounted for by summing the corrected day and night temperature images, using appropriate weighing coefficients. These coefficients were 0.25 and 0.75 for the daytime and nighttime scenes used by Coolbaugh et al. (2007a). The coefficients estimated from the AST_08 images in such a way, that the variance is reduced to a minimum, turned out to be in agreement with the coefficients obtained from ground-based measurements using thermocouples and infrared thermometers (Coolbaugh et al. 2007a; Eneva et al. 2007). To evaluate and subsequently remove the effect of thermal inertia from the satellite images, a combination of daytime and nighttime scenes is used that spans as short time as possible. ASTER pairs 12 hours apart (Coolbaugh et al., 2007a) and 36 hours apart (Eneva et al. 2006, 2007) were used for this purpose.

The procedure described is capable of achieving noise reduction and enhancement of some features that are not seen in the uncorrected images. Thus the model applied is potentially very effective in revealing and/or enhancing true thermal anomalies, while suppressing artifacts not related to geothermal activity.

2.2.5. Effect of Elevation and Thermal Inversions

The effect of topography is not limited to the slope aspect effect of surface temperature. With all other factors equal, both air and surface temperature generally decrease as the elevation increases. This is the reason that Figs. 2-1b and 2-3d, obtained after removal of the effects described in Sections 2.2.1-2.2.3 above, show warmer temperatures at lower elevations. This effect is more readily discernable at night. During the day, high temperature contrasts between sunlit and shaded areas can completely distort the effect of elevation. A theoretical adiabatic lapse rate of –9.8°C/km is cited in the meteorological literature (e.g., Chapman et al. 2001). So-called "environmental" lapse rate is lower, due mostly to the presence of water vapor, with –6.5°C/km assumed to be suitable in most cases. The temperature-elevation trend can be so pronounced in some cases that it has been possible to effectively use it as a surrogate to calculate missing elevation data (Crippen et al. 2007).

However, the above effect of elevation on surface temperature can be reversed due to the meteorological phenomenon of temperature inversion (e.g., Chapman et al. 2001), more frequently observed at night and in the winter. In relatively stable atmospheric conditions (i.e., low wind speed), a layer of cold air can form close to the surface that gets pulled by gravity, moving downward through drainage channels (so-called katabatic flow) until topographic or meteorological barriers are reached. As a result, the bottoms of valleys may become colder compared with higher elevations and thus temperature inversions take place. The increase of temperature with elevation may stop at the foot of hills and mountains, above which normal decrease of temperature with elevation develops. This may lead to formation of relatively warm belts at the foot of mountains. Temperature inversions can be sustained only at lower wind speeds, and if the winds are stronger, they do not get formed. Thus the same areas may exhibit such inversions on some nights, but not on others.

2.3. Orthorectification

The intention in this project was to study relatively large areas at once, hence the subject of orthorectification becomes more important compared with studies of relatively small areas without much elevation change, as done by Coolbaugh et al. (2007a). In the latter case, one can get away with simply co-registering the various images used (e.g., daytime and nighttime AST_08). However, when a larger region with varied topography is analyzed, it becomes much more obvious that the topographical variations of the surface of the earth and the tilt of the satellite sensor affect the distance with which features are displayed on the satellite image. The more topographically diverse the landscape, the more distortion inherent in the imagery. Such terrain displacement can be hundreds of meters. In order to accurately remove the image distortions, a digital elevation model (DEM) is used to perform image orthorectification.

The orthorectification task unexpectedly turned out to be a major technical hurdle in this project. The software used, ENVI from ITT Visual Information Solution (ITT VIS), claimed that it provides orthorectification of ASTER Level 1A and Level 1B. However, orthorectification of Level 2 products was needed, i.e. for AST_08 (temperature) and AST_07XT (reflection). At first, ITT provided technical assistance in the attempts to use the orthroectification of Level 1B as a basis for that of Level 2. After numerous trials, it became clear that the approach did not work properly. ITT then provided a plug-in specifically designed for ASTER Level 2 orthorectification. Initially it appeared to work, but then it turned out this was only true in cases when the look angle is 0, that is, when the scene is taken directly vertically down from the satellite platform. However, most ASTER imagery is acquired at non-zero look angles and then terrain distortions remained even after orthorectification attempts. Even though ITT included in their agenda to correct this error in ENVI's next update, this has not been done yet. As to other commercial software for processing of remote sensing images, no attempts have been made to tackle ASTER Level 2 at all (e.g., PCI Geomatics, ERDAS, ER Mapper). A freely available software from Caltech (COSI-Corr found at http://tecto.gps.caltech.edu/resources/index.htm) also provides orthorectification of only ASTER Level 1A. It appeared that in all cases, the main problem was that Level 2 is already geometrically altered, and a rigorous geometrical processing

such as orthorectification was considered unreliable. Also, it appeared there were problems with properly processing the orbital information.

After an extensive search of the technical literature, a method was finally identified (Wu 2008), so-called three-model method, that presumably did not need satellite orbital information and could perform orthorectification only using the image itself and ground control points (GCPs). The code creator, Dr. Wu from CSIRO, Australia, was contacted and although he had not worked with ASTER Level 2 data before, he agreed to try his code on a sample of the data used in this project. It turned out that his procedure worked, and it is likely the only one at present that is successful with this type of data. Dr. Wu has another related approach, the so-called affine method, which was also tried on the ASTER Level 2 data and seemed to perform slightly better than the three-model method. Therefore the affine method was chosen to be used in this project. It was fortunate for this project that Dr. Wu agreed to participate, at no cost to the Commission, as this fit well in the ongoing testing of his orthorectification codes. However, this process is going slowly and still continues, due to his involvement with CSIRO projects that are his primary obligation.

2.4. Field Trips

If any apparent temperature anomalies are identified from space, the ultimate verification would be on the ground. For this reason, several field trips were planned in this project. Some of them were carried out concurrently with the passage of the Terra satellite, during which the ASTER instrument acquired imagery. This was coordinated through the U.S. ASTER team and the Jet Propulsion Laboratory (JPL). The ground-based measurements that were collected in the field included surface temperature measurements with an infrared camera, measurements with temperature probes at 1-m and 2-m depths, and surface reflection measurements for albedo corrections. In addition, atmospheric radiosonde measurements were also taken during one of the field trips, with the intention to correct the satellite imagery for the presence of water vapor in the atmosphere (Tonooka 2001). More details are described in Section 3.5.

It is expected that ground-based surface temperature measurements are in reasonable agreement with the kinetic surface temperature calculated from the thermal infrared (TIR) bands after separation from emissivity. Only then can it be assumed that satellite data meaningfully reflect surface and subsurface processes. A rationale for this is provided by Allis et al. (1999), who compared shallow soil temperature measurements (at <1-m depth) in the Dixie Valley Geothermal Power Project (Nevada) with airborne TIR imagery, both taken prior to dawn in order to minimize solar heating effects from the previous day. Although the airborne TIR temperatures were on average cooler than the soil measurements, good correlation was observed between the two types of temperatures, indicating that anomalies in soil temperature would likely correspond to distinct anomalies of similar magnitude in the TIR measurements. This reasoning is likely extendable to satellite TIR as well, such as the one used in this project.

3.0 Project Results

3.1. Choice of ASTER Data

Numerous ASTER data collected over the central part of eastern California exist in the data archive. Nighttime images are of particular interest as described in Section 2.0. However, nighttime images were relatively lacking and many of the existing nighttime scenes were rather cloudy. Also, only a few nighttime/daytime pairs were identified, as such pairs are not commonly collected without special ordering. Still, a pair was identified over the Coso geothermal field from August 2001, and was the first to be analyzed. Additional nighttime images were collected through a Data Acquisition Request (DAR) and arrangements were made for collection of daytime/ nighttime pairs of scenes. A number of scenes were collected and downloaded, of which the best subset for analysis was chosen, with optimal spatial and daytime/nighttime coverage. Table 3.1 shows a list of these chosen scenes. Each scene listed in this table is represented by two products (AST_08 and AST_07XT) if it is a daytime scene, and one product (AST_08) if it is a nighttime scene. Figure 3.1 shows the overlapping areas from these daytime/nighttime pairs, with a distinction between 12-hr and 36-hr pairs.

Table 3-1. A list of best ASTER image pairs for the study region

Day-Night Overlaps	ASTER ID	Area	Time
2006-Aug-21	L1A#00308212006055958	Coso	Night
2006-Aug-21	L1A#00308212006060007	Coso	Night
2006-Aug-21	L1A#00308212006060015	Coso	Night
2006-Aug-21	L1A#00308212006060024	Coso	Night
2006-Aug-22	L1A#00308222006184452	Coso	Day
2006-Aug-22	L1A#00308222006184501	Coso	Day
2006-Aug-22	L1A#00308222006184510	Coso	Day
2006-Aug-22	L1A#00308222006184518	Coso	Day
2001-Jun-28	L1A#003_06282001185917	Monache	Day
2001-Jun-28	L1A#003_06282001185926	Monache	Day
2001-Jun-29	L1A#003_06292001060219	Monache	Night
2001-Jun-29	L1A#003_06292001060228	Monache	Night
2008-Jul-1	L1A#00307012008185126	Long Valley	Day
2008-Jul-2	L1A#00307022008055511	Long Valley	Night
2008-Jul-2	L1A#00307022008055520	Long Valley	Night
2000-Jul-12	L1A#003_07122000060919	Panamint Valley	Night
2000-Jul-12	L1A#003_07122000060927	Panamint Valley	Night
2000-Jul-13	L1A#003_07132000185430	Panamint Valley	Day
2000-Jul-13	L1A#003_07132000185439	Panamint Valley	Day
2000-Jun-10	L1A#003_06102000060936	Tecopa	Night
2000-Jun-10	L1A#003_06102000060944	Tecopa	Night
2000-Jun-11	L1A#003_06112000185429	Tecopa	Day
2000-Jun-11	L1A#003_06112000185438	Tecopa	Day

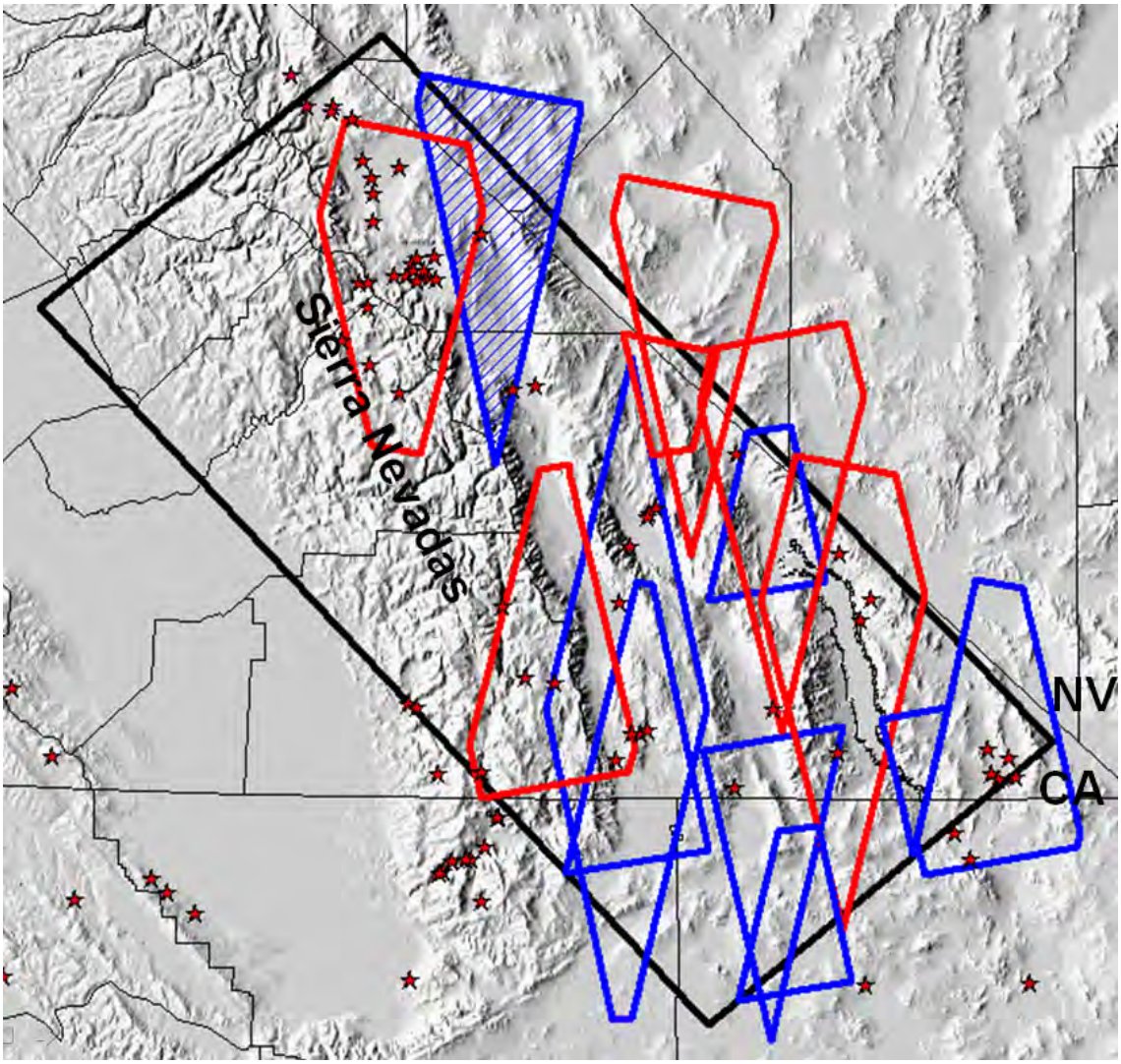

Figure 3-1. Spatial coverage from the available daytime/nighttime ASTER image pairs. Study area is outlined in black. Red stars mark hot springs. Red boundaries delimit the overlap areas of daytime and nighttime images acquired on the same day (i.e., 12 hours apart). Blue boundaries delimit overlaps of daytime and nighttime images acquired 36 hours apart. Coverage in the hatched blue area is incomplete because of partial clouds. The width of the figure is 450 km.

3.2. Orthorectification

Orthorectification is crucial when the study region is characterized by variable elevation. Figure 3-2 demonstrates this variability for the main study area in this project, the Coso geothermal field. Initially, an approximate method was used to accommodate the topographic challenges, where an orthorectified ASTER Level 1B TIR was used to determine tie-points in a pair of daytime and nighttime AST_08, and the AST_07 corresponding to the daytime AST_08. Once orthorectification became available through Dr. Wu, the systematic processing of the images listed in Table 3-1 began. Nine ground control points (GCPs) were determined for the AST_08 and AST_07XT products of the scenes listed in Table 3-1.

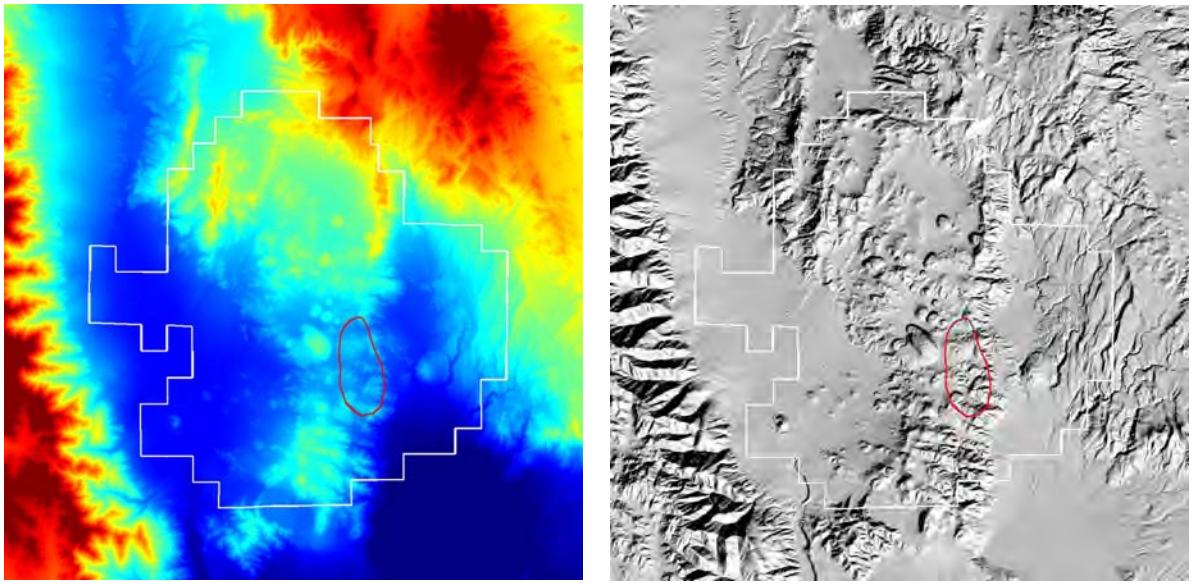

Figure 3-2. Topographic variability in the Coso geothermal area. Elevations from 700 m to 2700 m. White outline marks the KGRA (known geothermal resources area). Red outline marks the production area. Left – elevations in color, with increasing elevation from blue to red. Right – shaded relief. Size of area shown is 36 km x 36 km. Elevation data from USGS (http://seamless.usgs.gov).

It was determined that nine GCPs distributed evenly throughout each image, are optimal for successful orthorectification. All AST_07XT and some AST_08 products are already orthorectified, but most AST_08 are still in the pipeline. Table 3-2 shows examples of the RMS (root-mean squares) for the GCPs in the orthorectifed scenes. The residuals for the individual GCPs are also shown. These results are rather good, because the RMS from all nine points, and most of the individual residuals(in X and Y in the table), are smaller than the pixel size, 15 m for the AST_07XT and 90 m for the AST-08 products. Although less accurate than AST_07XT and daytime AST_08, the orthorectification of the nighttime AST_08 imagery is still good, although it is more difficult to determine GCPs in nighttime imagery.

Table 3-2. Examples of residuals and RMS from orthorectification

Nighttime AST_08 (temperature)			Daytime AST_08 (temperature)			AST_07XT (reflection)		
	X	Y		X	Y		X	Y
res(X,Y)	62.112	-41.337	res(X,Y)	9.889	-32.201	res(X,Y)	14.894	-19.53
res(X,Y)	-33.755	51.779	res(X,Y)	-5.474	-22.39	res(X,Y)	-4.278	15.35
res(X,Y)	-19.118	57.366	res(X,Y)	-19.045	10.874	res(X,Y)	3.24	13.995
res(X,Y)	-17.61	-48.824	res(X,Y)	-9.413	14.512	res(X,Y)	-12.39	-1.046
res(X,Y)	-40.71	18.745	res(X,Y)	14.584	5.012	res(X,Y)	-6.026	-5.949
res(X,Y)	19.986	-25.765	res(X,Y)	-1.904	10.916	res(X,Y)	7.597	-2.63
res(X,Y)	27.211	10.038	res(X,Y)	6.636	6.761	res(X,Y)	-6.334	2.47
res(X,Y)	-3.224	-22.359	res(X,Y)	-7.299	4.145	res(X,Y)	3.681	-1.289
res(X,Y)	5.1	0.357	res(X,Y)	4.621	2.37	res(X,Y)	-0.374	-1.371
RMS(X,Y)	**30.744**	**36.025**	**RMS(X,Y)**	**10.078**	**15.202**	**RMS(X,Y)**	**7.831**	**9.809**

3.3. Imagery Corrections

Figure 3-3 shows ASTER Level 1 B TIR scenes of size ~60 km x 60 km are from a day-time/nighttime pair partially covering the Coso Geothermal Power Project. The daytime scene was taken on 08/24/2001, at 11:52 a.m. local daylight saving time (i.e., 10:52 a.m. PST). The nighttime scene was taken prior to the daytime scene, on 08/22/2001, at 11:06 p.m. local daylight saving time (i.e., 10:06 p.m. PST and 6:06 a.m. on 08/23/2001 GMT time, hence the title of the nighttime scene in Fig. 3-3 indicates the next day).

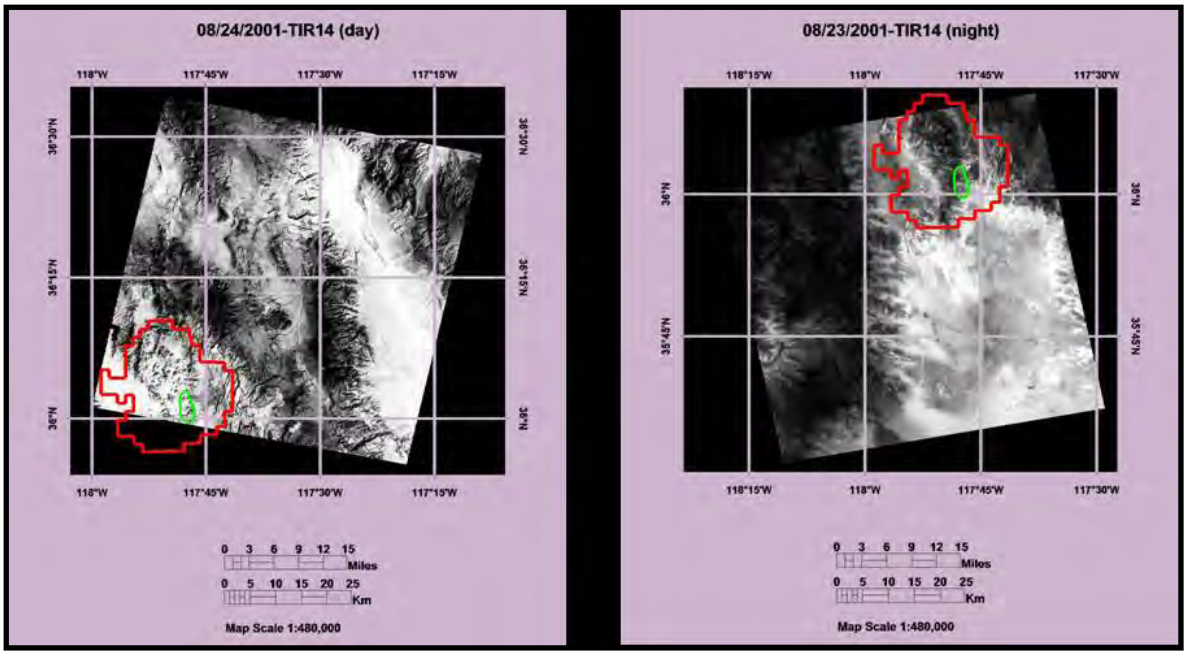

Figure 3-3. Level 1B TIR band 14, daytime (08/24/2001) and nighttime (08/22/2001). Coso KGRA and production area are outlined in red and green, respectively.

Figures 3-4 and 3-5 show daytime and nighttime AST_08 images (surface temperature derived from Level 1B TIR) collected in August 2006, as part of a field trip, where ground-based measurements were done concurrently with the satellite passages. More details on that field trip are given in Section 3.5.2 below.

The importance of taking into account the changing amount of heat through the course of a day is demonstrated in Figure 3-6. The so-called *shaded relief* is calculated from a digital elevation model (DEM). The shaded relief depends on the incident angle of solar irradiation and is the cosine of the angle between the surface normal and the sun's rays. Its value is between 0 and 1, with 1 indicating maximum possible heat flux. The scenes in Fig. 3-6 zoom in on an area around a small topographic feature, a Quaternary rhyolite dome (diameter < 1 km), showing the shaded relief at different times. It is evident that for any given pixel, depending on its location in respect to the local topography, the amount of solar heating could be different from that received by adjacent pixels, and changes during the day.

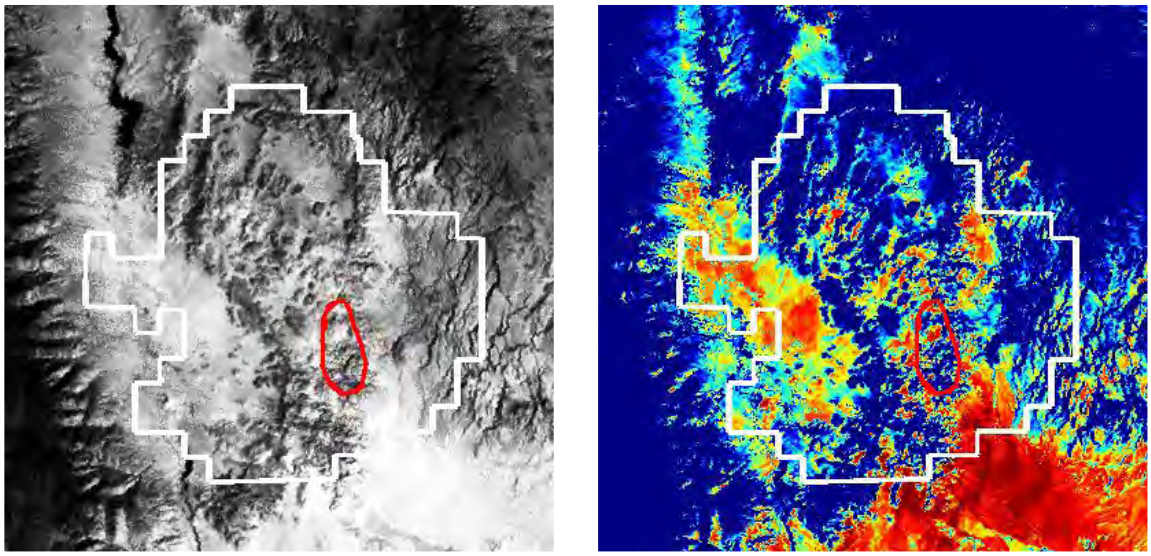

Figure 3-4. Daytime AST_08 collected over the Coso geothermal field in August 2006. Surface temperatures increase from dark to bright (left) or blue to red (right), and range between 21° C and 66° C. The Coso KGRA and the production area are outlined with white and red, respectively.

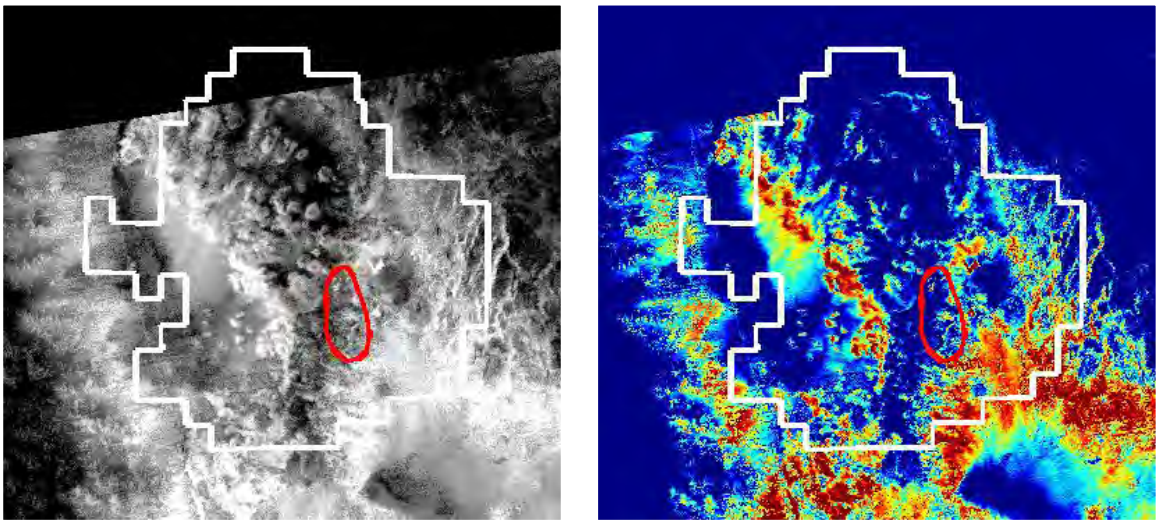

Figure 3-5. Nighttime AST_08 collected over the Coso geothermal field in August 2006. Surface temperatures range between 5° C and 36° C. Notations like in Fig. 3-4.

The simplified model described in Section 2.2.4 approximately accounts for heat dissipation and was used to calculate pseudo-temperature images to be subtracted from the AST_08 (surface temperature) images collected on 08/24/2001 (daytime) and 08/22/2001 (nighttime). The uncorrected and corrected nighttime AST_08 (surface temperature) images are compared in Figure 3-7. The whole area is known to contain surface manifestations of geothermal energy, so it is not surprising that "red" (i.e., "hot") areas are seen throughout the images. However, noise reduction is observed after correction and several features appear that

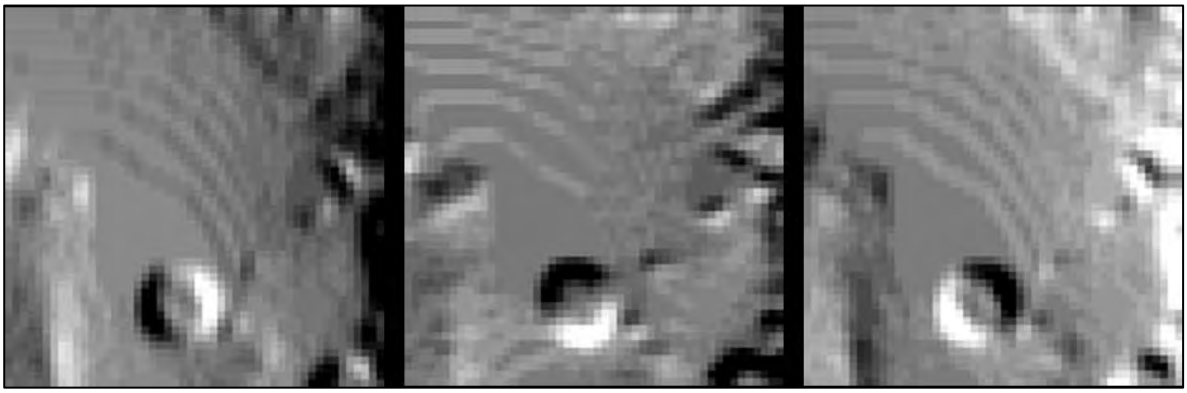

Figure 3-6. Example of changes in solar irradiation in the course of a day, depending on the topographic slope aspect. Circular feature is a rhyolite dome with a diameter of ~1 km in the Coso geothermal field. Increasing brightness indicates more solar irradiation, which would result in higher surface temperatures on satellite TIR images. From left to right - shaded relief one hour after sunrise, 6 hours after sunrise/7 hours before sunset, and 4 hours before sunset. Note migration of high temperatures from the eastern, through the southeastern, to the southwestern slopes of the dome. After Eneva et al. (2006).

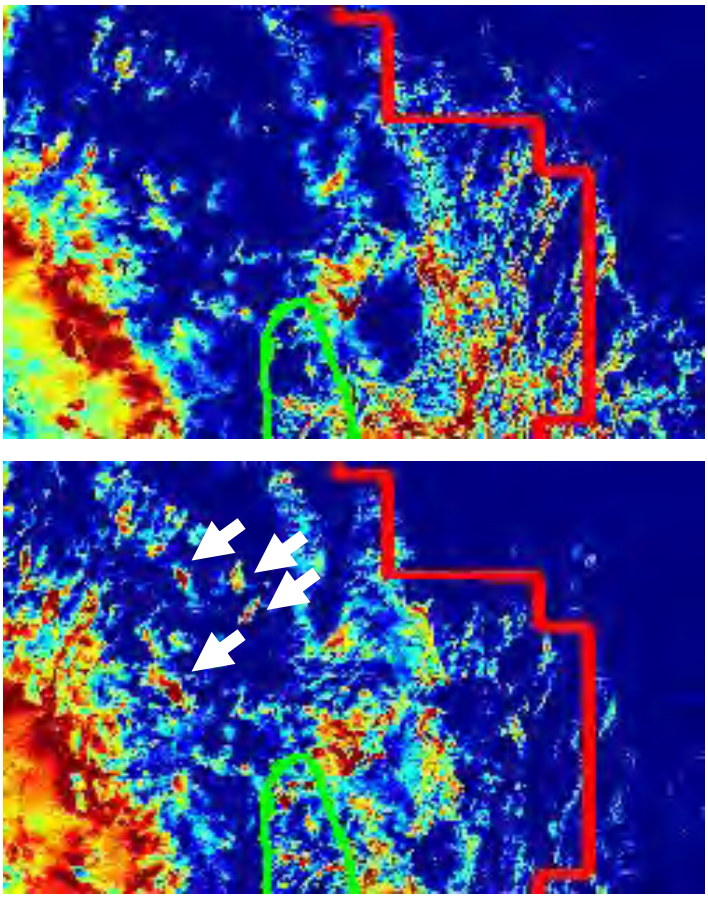

Figure 3-7. Comparison of the uncorrected nighttime AST_08 (top) with the corrected one (bottom), from the overlapping area of the image pair shown in Fig. 3-3. Red and green outline mark Coso KGRA and the production area, respectively. White arrows show some of the temperature anomalies seen only in the corrected image.

are not seen in the uncorrected age. These results show that though simplified, the model applied here is potentially very effective in revealing and/or enhancing some thermal anomalies and suppressing false thermal anomalies. Correction,for thermal inertia, was also performed. The weighing factor that produced minimum variance was found to be 0.624 for the nighttime image (and consequently, 0.376 for the daytime image). That is, the combined scene with minimal effect of thermal inertia contains about 2/3 of the nighttime and 1/3 of the daytime scene. This is

different from the 0.75:0.25 ratio used by Coolbaugh et al. (2007a) in Nevada, so these factors have to be identified individually for each daytime/nighttime pair.

Figures 3-8 and 3-9 draw attention to individual small areas from Fig. 3-7. Revealing of some features that are not seen before correction is evident. Figure 3-10 shows a corrected AST_08 from August 2006, where the main known hot areas at Coso are evident – Coso Hot Springs (CHS), Devil's Kitchen (DK), and Wheeler (WH).

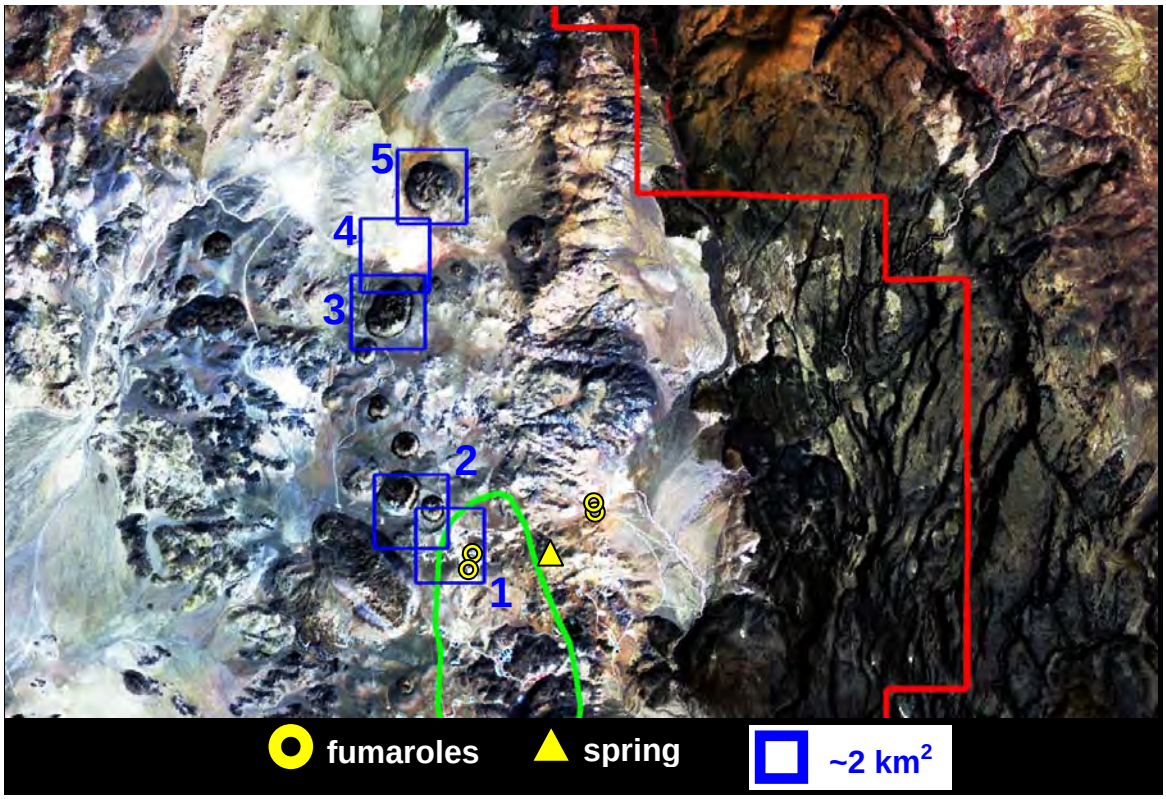

Figure 3-8. Level 1B VNIR radiance in RGB (red-green-blue) for the area of overlap between the daytime and nighttime TIR scenes from Fig. 3-3. R=band 3, G=band 2, and B=band 1. Yellow circles indicate fumaroles and yellow triangle shows a hot spring. Blue squares mark features of interest: 1 – two fumaroles and an open pit mine in between; 2, 3, and 5 – rhyolite domes; 4 – dry lake.

Broad areas of elevated temperatures are seen in Figs. 3-7 (August 2001) and 3-10 (August 2006) that are not necessarily associated with geothermal activity. Such features may be related to the effect of elevation (generally warmer temperatures at lower elevations) and microclimate (e.g., temperature inversions producing warmer surface temperatures in valleys), discussed next in Section 3.4. Vegetation can also create apparent cooler areas that make adjacent bare ground areas look warmer. However, in the Coso geothermal field this effect is minimal (Figure 3-11).

Figures 3-12 and 3-13 show more examples, from the Mammoth area to the north, on the other edge of the study region. A number of nighttime images are available for this area that

show some persistent warm features even with changing seasons, as well as possible seasonal variations and/or changes with time.

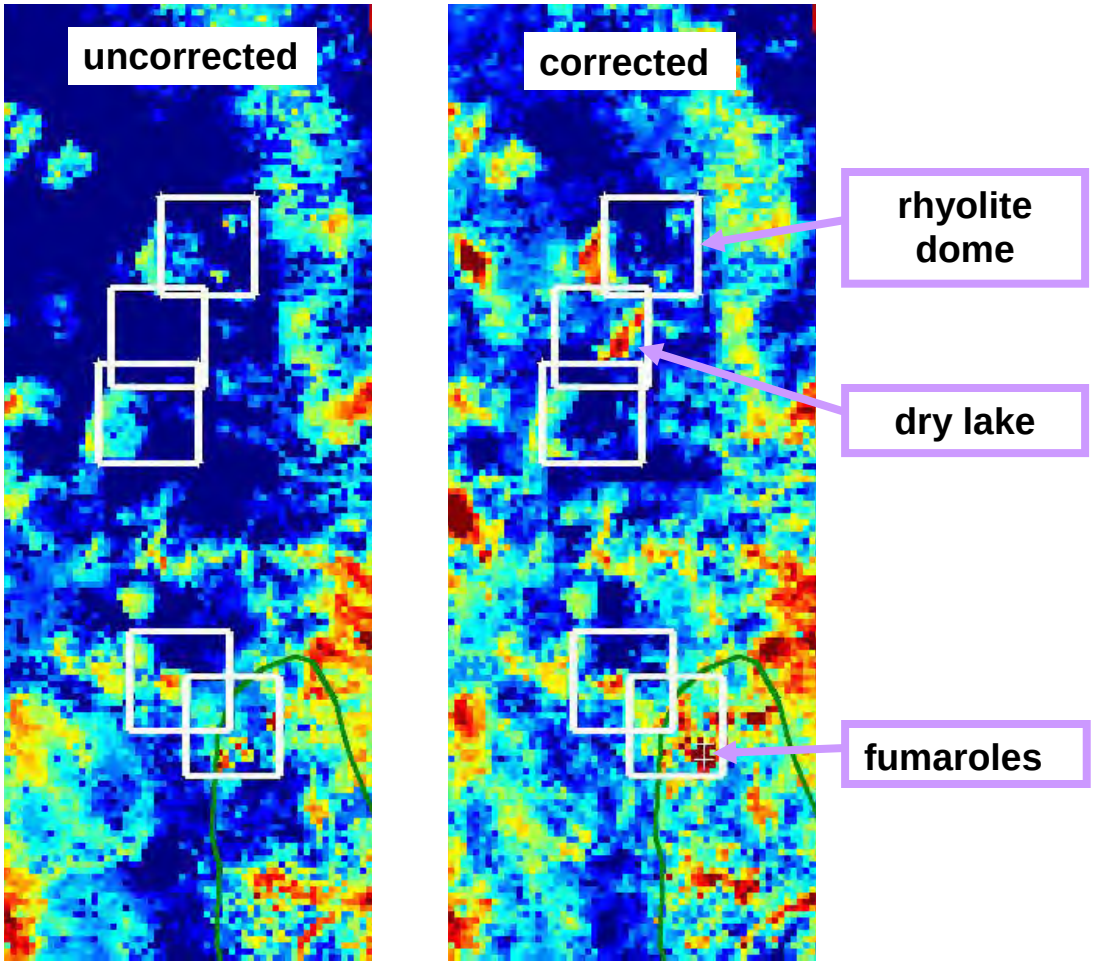

Figure 3-9. Comparison of nighttime uncorrected and corrected AST_08 images (surface temperature) in the Coso geothermal field for the five areas marked in Fig. 3-8 (here outlined with white). Blue through yellow to red indicate increasing surface temperatures. Dark green outline denotes the production area. Note the differences around the two fumaroles and the dry lake, where elevated temperatures are only seen in the corrected image.

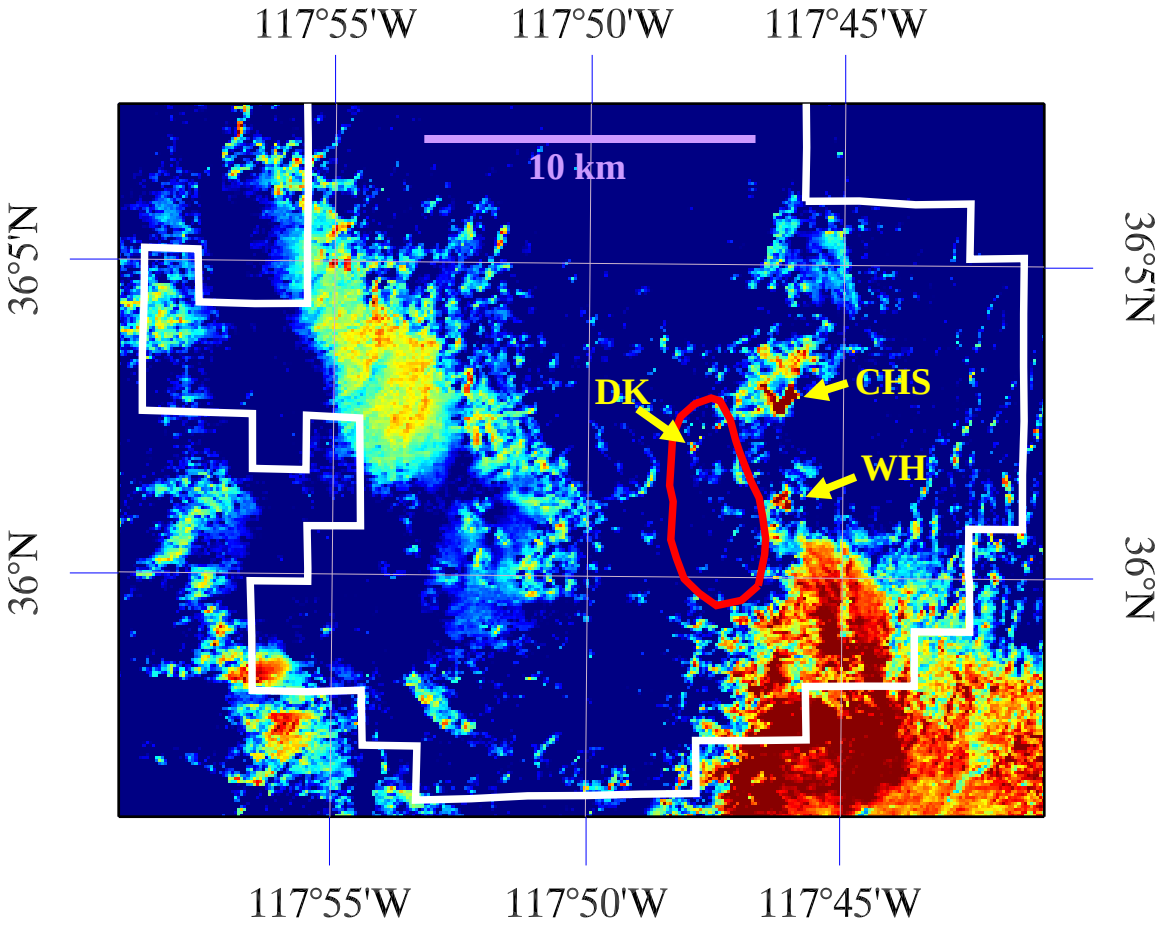

Figure 3-10. Corrected AST_08 (surface temperature) in the overlapping area of the day-time/nighttime pair from August 2006 (Figs. 3-4 and 3-5). White and red outlines mark KGRA and production areas, respectively. Blue to red indicate increasing temperatures. The CHS and WH areas are clearly captured as anomalies with elevated temperatures (yellow arrows), and the DK area is also suggested. Broad areas of higher temperatures are associated with topographic planes and valleys with likely nighttime temperature in-versions (see Section 3.4 below).

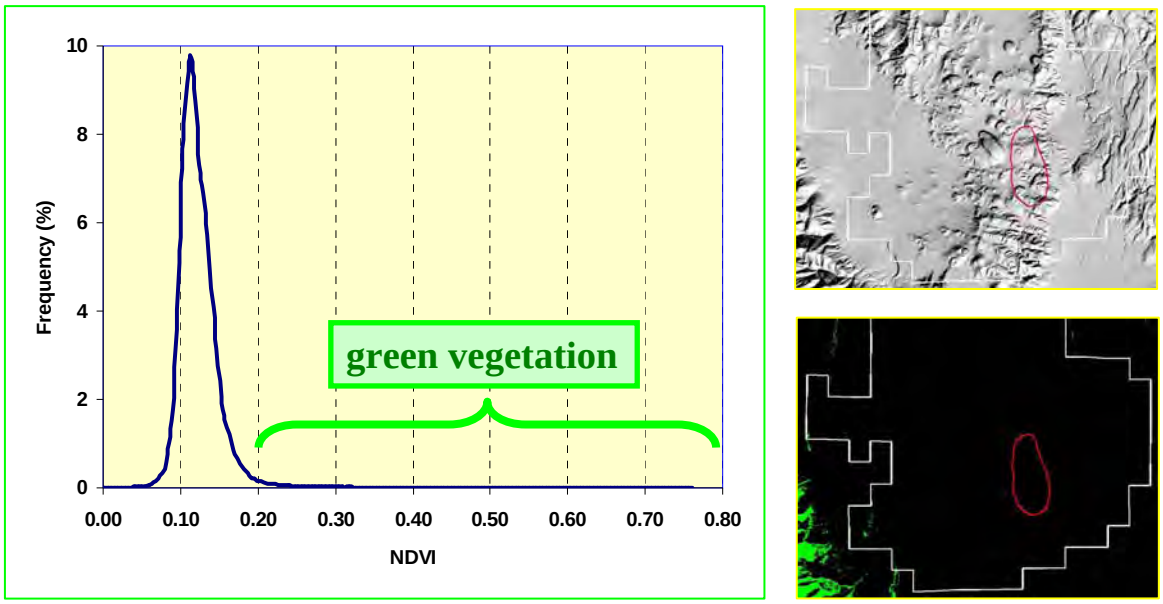

Figure 3-11. Vegetation index, NDVI = (band3 – band2)/(band3 + band2), for the Coso area. Most values are below 0.2 indicating little green vegetation. Top right – shaded relief. Bottom right – map of NDVI showing areas with NDVI > 0.2 in green. KGRA and production area are outlined with white and red, respectively.

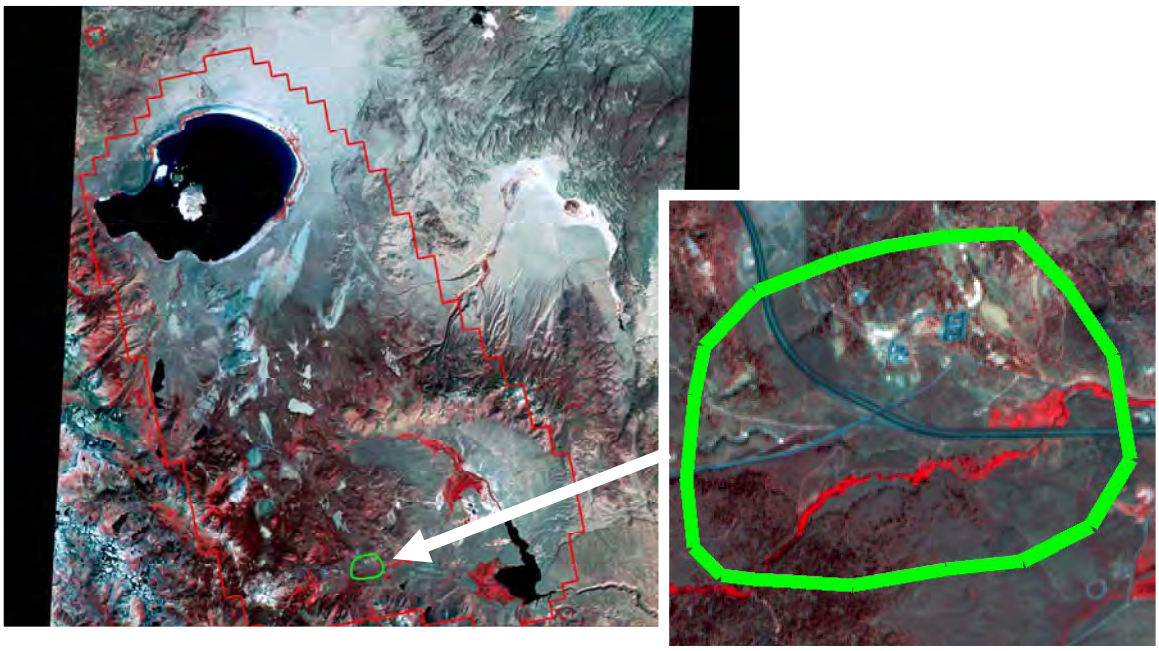

Figure 3-12. ASTER Level 1B VNIR (shown in RGB) from the Mammoth area. Image from September 2005. KGRA and production area outlined in red and green, respectively.

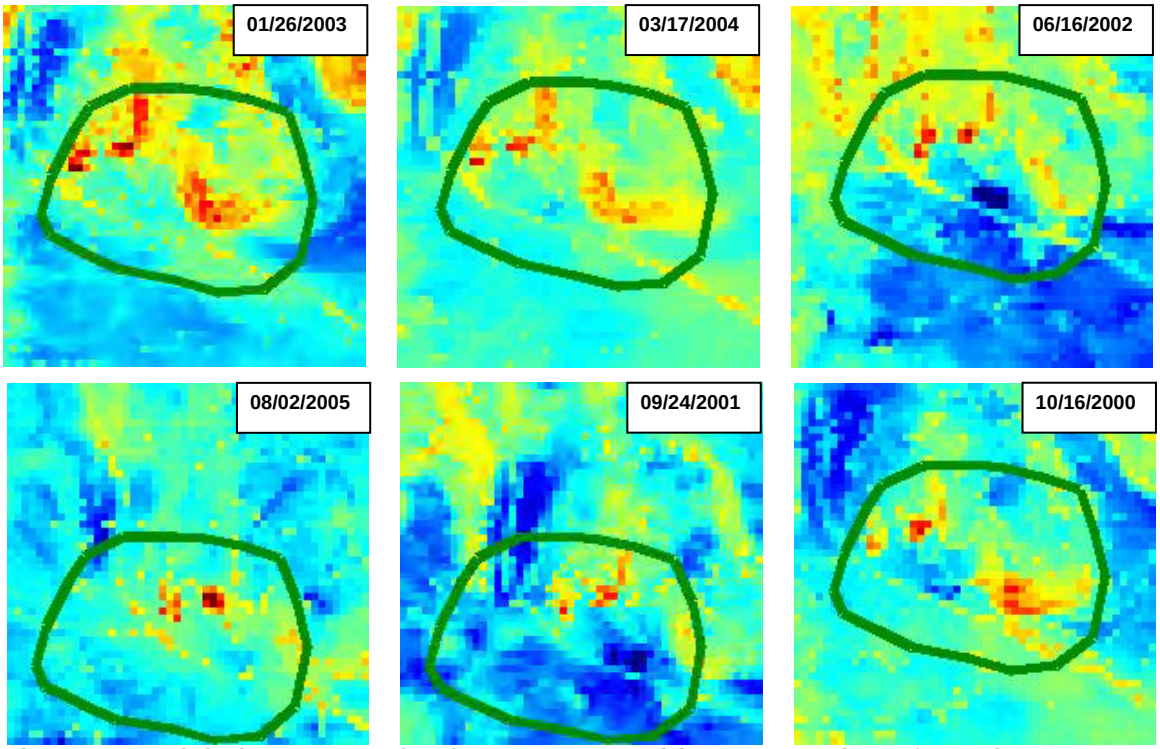

Figure 3-13. Nighttime AST_08 (surface temperature) images over inset from Fig. 3-12. Dates of image collection are marked in upper right corner of each plot. Green outlines mark production area. Temperature increases from blue to red.

3.4. Effects of Elevation and Temperature Inversions

With all other factors equal, both air and surface temperatures generally decrease as the elevation increases. This effect is more readily discernable at night. During the day high temperature contrasts between sunlit and shaded areas can significantly distort the effect of elevation. Therefore, it is likely best to correct for the elevation effect after the effects of albedo and topographic slope and aspect are removed. A theoretical adiabatic lapse rate is commonly cited in the meteorological literature as –9.8°C/km (e.g., Chapman et al., 2001). The so-called "environmental" lapse rate generally observed in nature is lower, due mostly to the presence of water vapor, with –6.5°C/km assumed to be suitable in most cases. The temperature-elevation trend can be so pronounced in some cases that it has been possible to effectively use it as a surrogate to calculate missing data in digital elevation models (Crippen et al. 2007).

Figures 3-14 to 3-17a-c show temperature-elevation plots from the Coso geothermal field, in which the decrease of surface temperature with elevation is a dominant trend. The surface temperatures are taken from AST_08 images with spatial resolution of 90 m, while the elevations are from USGS digital elevation models (DEM) with spatial resolution of 30 m (downloaded from http://seamless.usgs.gov). Nighttime and daytime AST_08 covering the same area are shown in Figs. 3-14 and 3-15, respectively. The nighttime lapse rate of about –5°/km indicated by the slope of the straight line in Fig. 3-14 is lower than the expected envi-

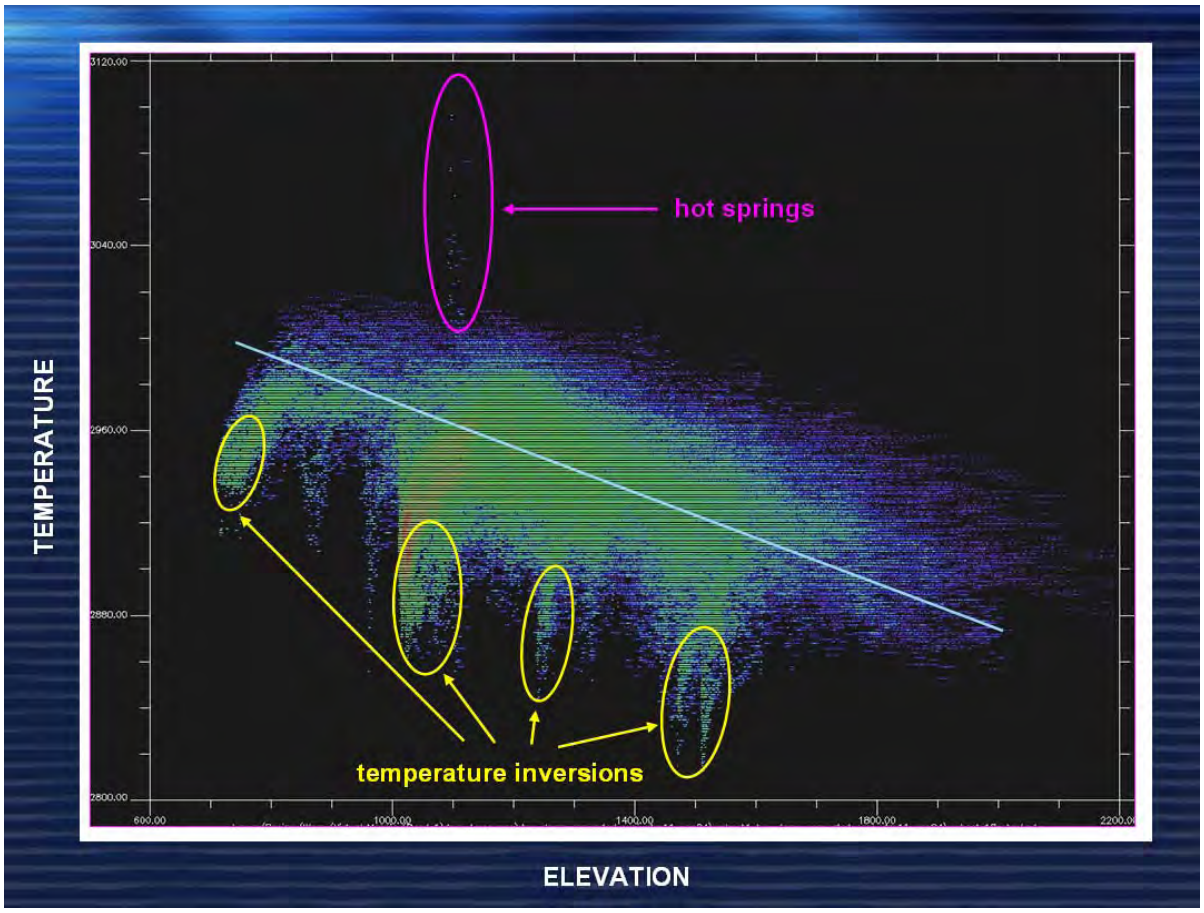

Figure 3-14. Nighttime density plot of surface temperature versus elevation extracted from a nighttime AST_08 image collected over Coso in August 2006. Temperature inversions (yellow outlines) are superimposed on the normal temperature decrease with elevation (average trend is approximated by the light blue straight line). Hot springs and fumaroles have a distinct range of high temperatures not dependent on elevation (pink outline). From Eneva and Coolbaugh (2009) and Quattrochi et al. (2009).

ronmental lapse rate of –6.5°C/km (e.g., Crippen et al. 2007), likely due to temperature inversions (discussed below) superimposed on the usual temperature-elevation trend. Away from temperature inversions, the lapse rates are spatially varying, between –5.4°/km and as high as –9.8°/km, which is the adiabatic lapse rate.

Fig. 3-15 shows a similar plot, but from the daytime AST_08. In this case the average lapse rate over the whole area represented by the slope of the straight line is –8.4°C/km. However, due to high contrasts in solar irradiation for some portions of the area covered by AST_08, there are some very steep temperature-elevation relationships, with slopes up to –30°C/km. This underlines the necessity to eliminate the differential effects of slope and aspect before attempting to derive credible lapse rates from daytime TIR imagery. Unlike the nighttime, the daytime temperature-elevation relationship is not contaminated by temperature inversions.

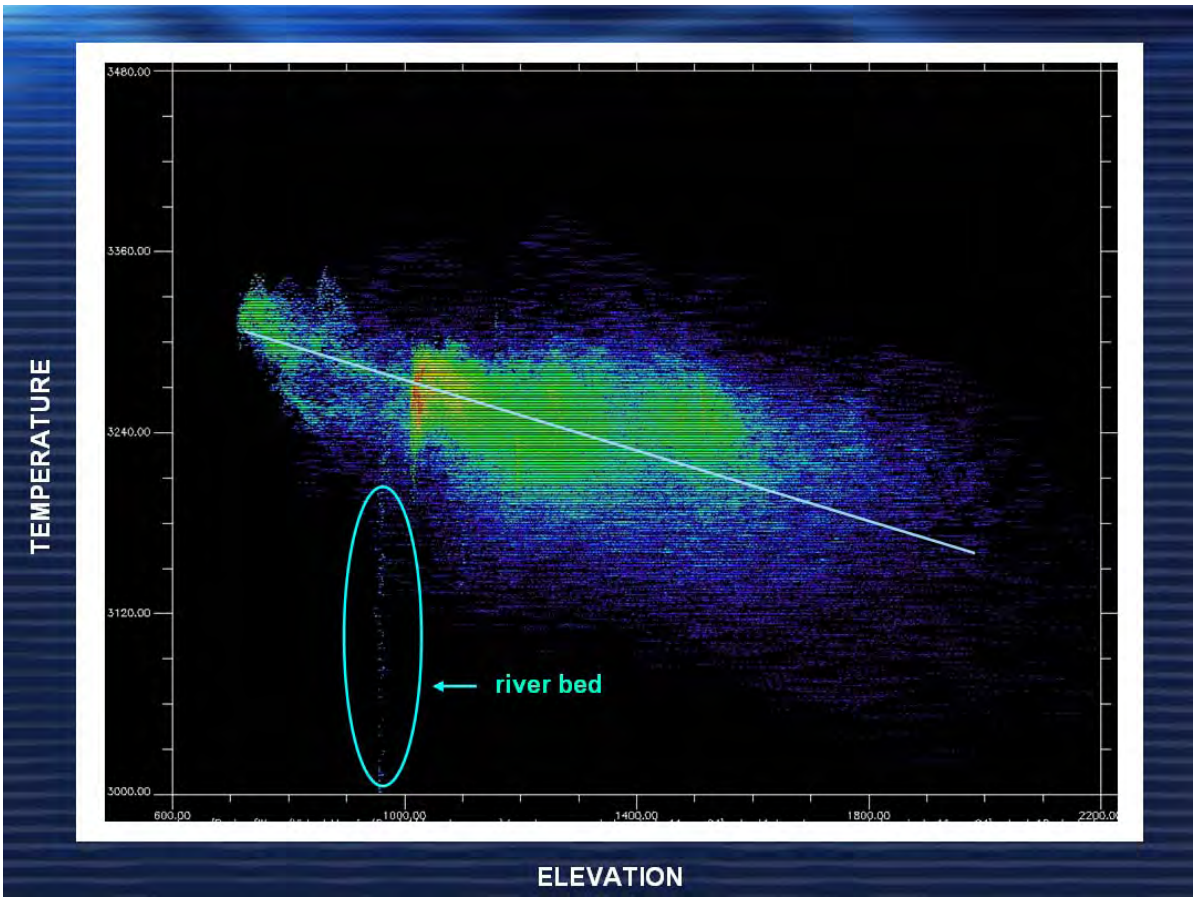

Figure 3-15. Daytime density plot of surface temperature versus elevation extracted from a daytime AST_08 image covering the same area as in Fig.3-14. Normal temperature decrease with elevation (average trend is approximated by light blue straight line) is not contaminated by temperature inversions. Hot springs are not evident either. A river valley is represented by a range of low temperatures not dependent on elevation.

The normal effect of elevation on surface temperature can be reversed due to the meteorological phenomenon of temperature inversions (e.g., Chapman et al. 2001), more frequently observed at night and in the winter. Figures 3-14, 3-16, and 3-17 illustrate these effects, as derived from nighttime AST_08. Such inversions are possible during the day as well, but mostly in winter. The AST_08 images used here are from the summer (month of August), so the daytime AST_08 does not show the presence of temperature inversions (Fig. 3-15).

Fig. 3-14 shows several temperature inversions superimposed on the normal temperature-elevation trend. It also shows how hot springs appear in this type of representation, as a wide range of high surface temperatures at a constant elevation. One can envision using such quick temperature-elevation plots in a search for hot springs in nighttime TIR images over isolated and difficult-to-access areas. Such plots may be also helpful even if geothermal temperature anomalies are more subtle, but the effects of albedo and topographic slope/aspect would have to be removed, in order to reduce the scatter seen in Fig. 3-14.

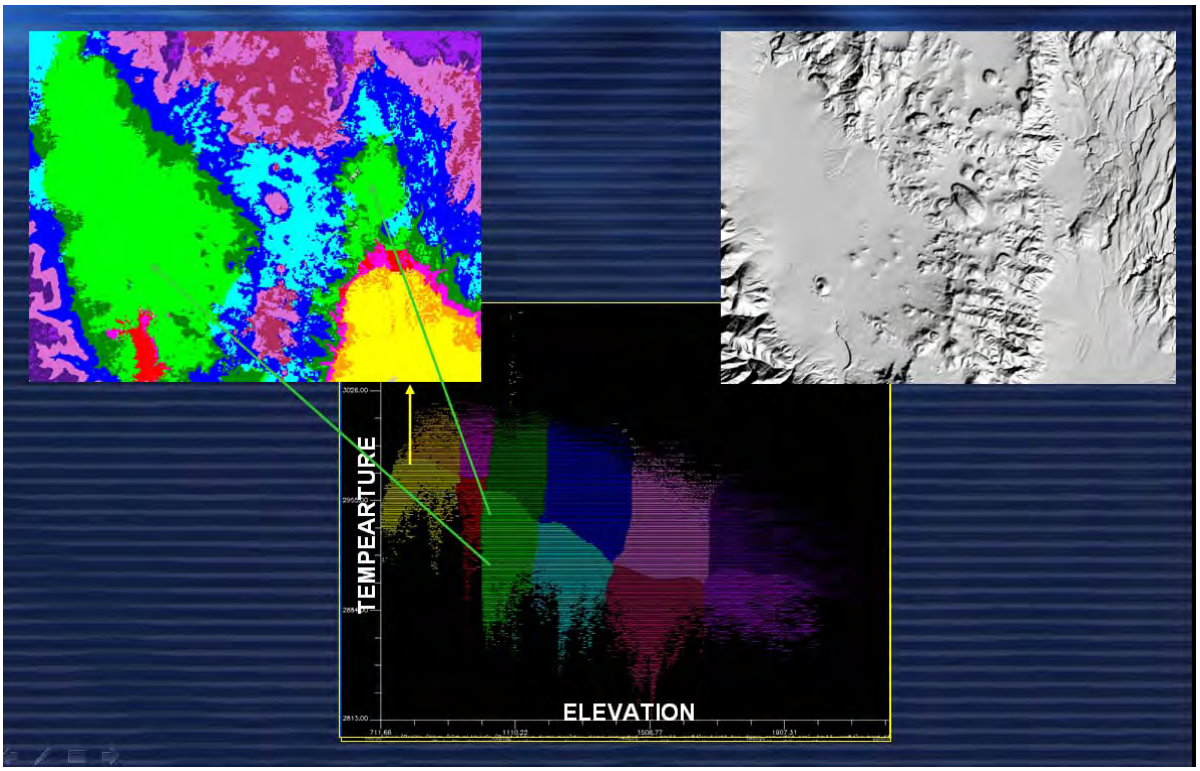

Figure 3-16. Map representation of the nighttime temperature inversions. Temperature-elevation plot is same as in Fig. 3-14, but divided in color sections to identify corresponding areas on map. Inset in the top right shows map of shaded relief in the area of the Coso geothermal field. Inset in the top left shows the same map but with color coded temperatures from the nighttime AST_08 image, with temperatures increasing from blue to red.

The temperature-elevation scatter plot shown in Fig. 3-16 is the same as that in Fig. 3-14, however different parts are colored with the same colors as the areas in a map that correspond to these parts of the plot. It is evident that certain portions of the plot, including the temperature inversion branches, correspond to spatially coherent areas in the map rather than being spatially scattered throughout the image.

Three examples of individual sub-areas with nighttime temperature inversions are shown in Fig. 3-17. The two distinct inverted branches A and B coming prominently out of a normal temperature-elevation trend (Fig. 3-17a), correspond to areas on both sides of a ridge. The same hot spring anomaly seen in the more generalized plot in Fig. 3-14 is easily attributable here to the Coso Hot Springs area (Fig. 3-17b). The third example is from a part of the area with the lowest elevations, where a valley transitions into higher elevations (Fig. 3-17c).

The above examples show that nighttime temperature inversions are quite common. It is thus imperative to take them into account, along with the effects of elevation, when satellite thermal infrared imagery is used to search for surface temperature anomalies attributable to subsurface processes, such as geothermal activity.

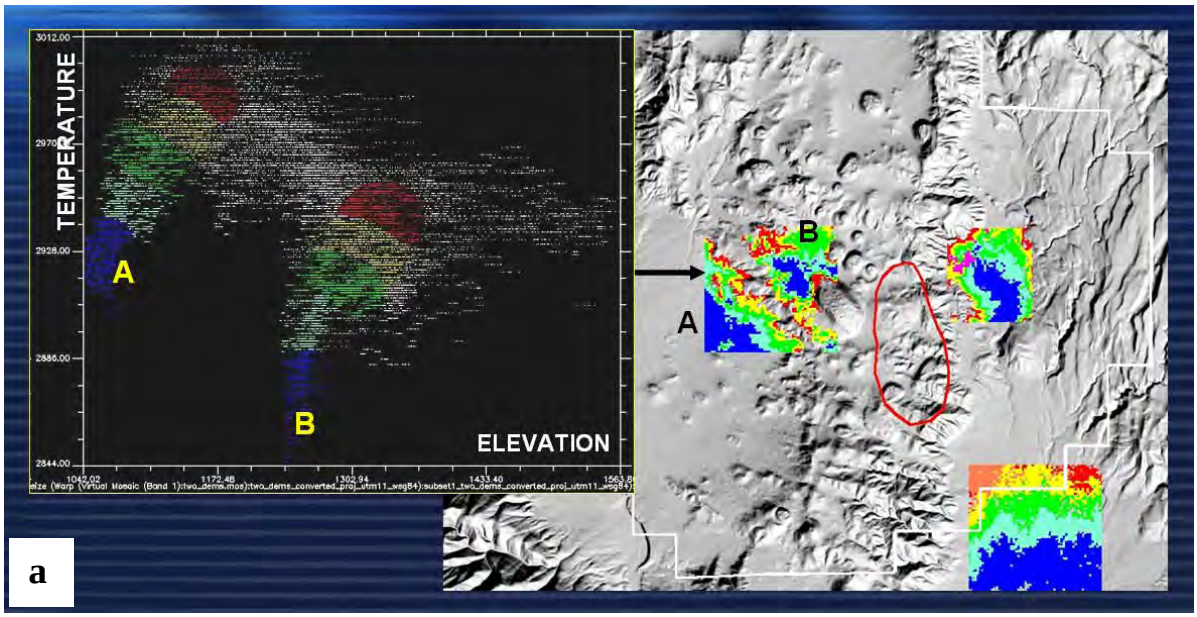

Figure 3-17. Examples of nighttime temperature inversions from ASTER TIR imagery. Plot to the right shows a map of shaded relief at the Coso geothermal field (same as in Fig. 3-16). White and red outlines mark the KGRA and the production area, respectively. Colored rectangles denote areas with nighttime inversions; temperatures increase from blue to red. Plot to the left shows temperature versus elevation, with the colored areas corresponding to the colors from the map of shaded relief. (a) An area east and north-east from Sugar Mountain. Note two distinct branches A and B superimposed on normal decrease of temperature with elevation. These temperature inversions developed on both sides of a ridge as seen from the map. (b) An area including the Coso Hot Springs (CHS) marked by pink color for the highest temperatures (also seen in Fig. 3-14). (c) A valley in the south-eastern corner of the map.

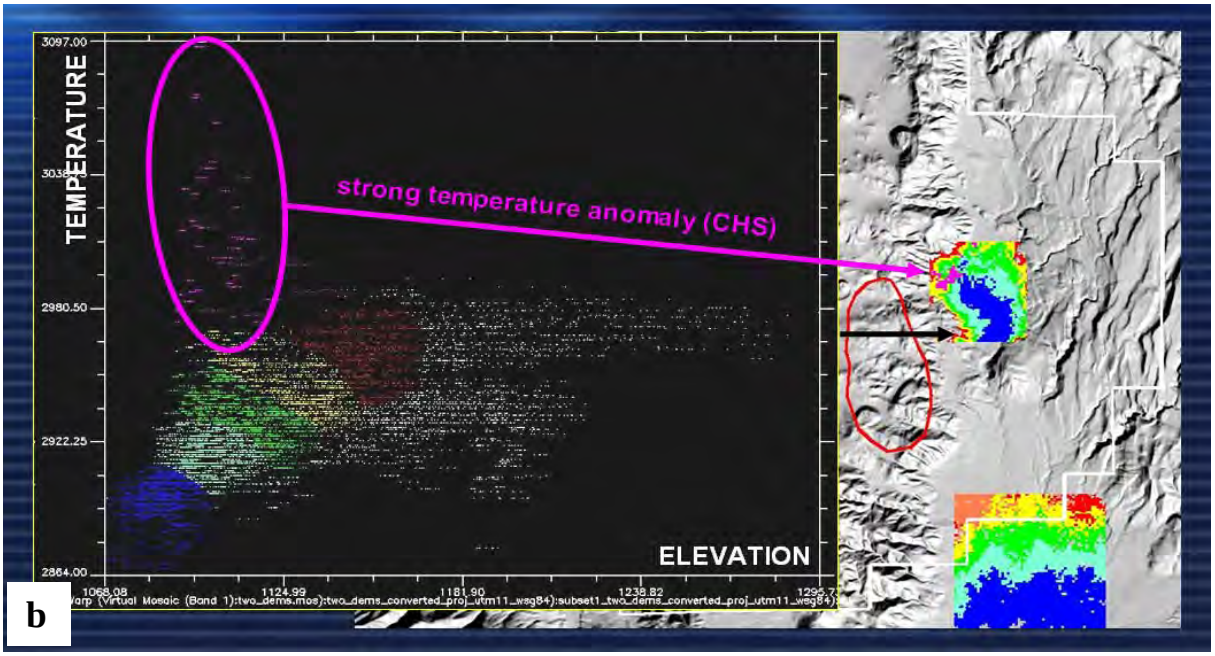

Figure 3-17 continued (b)

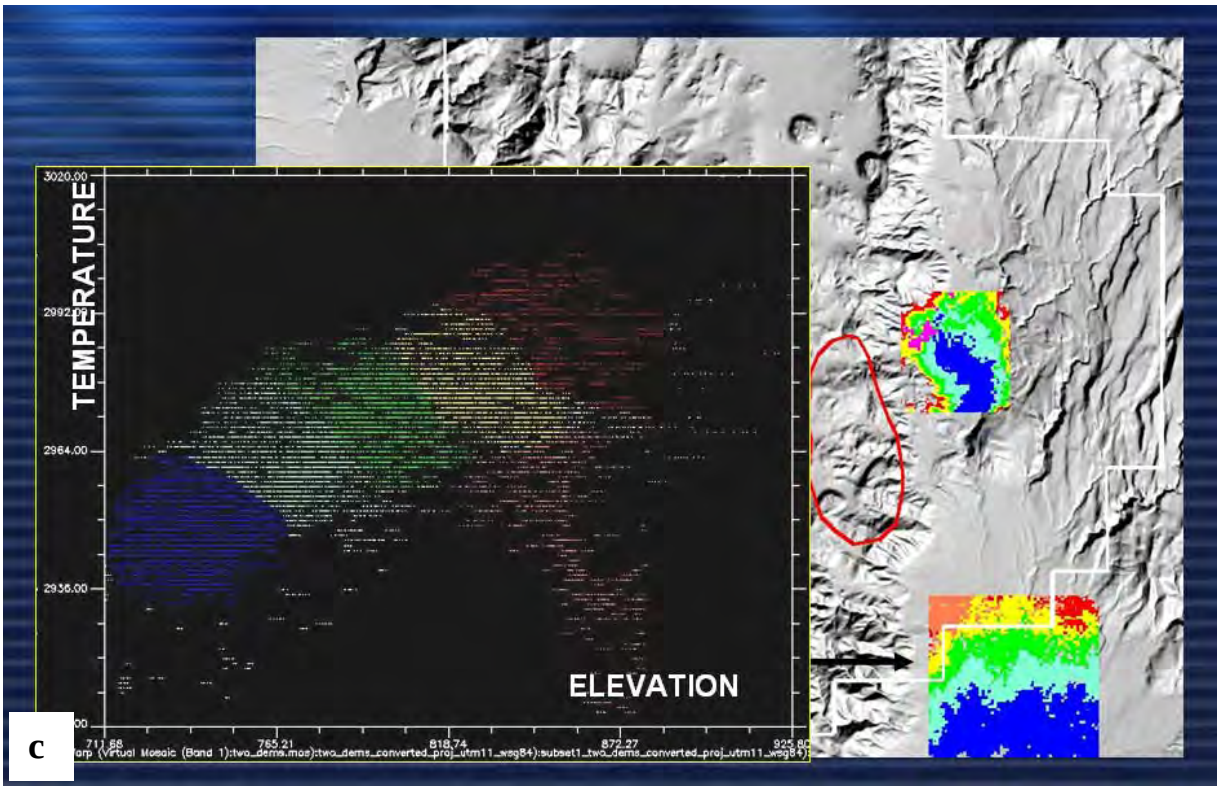

Figure 3.17 continued (c)

3.5. Field Trips

Two field trips took place in the summer of 2006, while attempting to make ground-based measurements concurrently with the passage of the Terra satellite, when ASTER acquired imagery over the Coso geothermal field. Arrangements were made with the Jet Propulsion Laboratory (JPL) for collections of daytime/nighttime pairs, 36 hours apart. The first field data were collected in July 2006. Because of the poor quality of the concurrently collected ASTER images at that time, a similar field trip was scheduled 32 days later, during another passage of the satellite in August 2006. In addition, two campaigns of 2-m temperature probe measurements took place in eight valleys in astern California, in May and June of 2009.

3.5.1. July 2006

Due to the cloudy ASTER data collected during the first field trip, the imagery could not be used. However, several concurrent ground-based measurements took place at that time, and while there was no good satellite imagery to compare them with, they depict interesting aspects of the Coso geothermal field. Also, these measurements are instructional for what is possible, and what could be done in future field experiments of this type.

Temperature loggers were used to record subsurface temperatures in 13 locations grouped along three lines across distinct hydrothermal features in the Coso Hot Springs (CHS), Devil's Kitchen (DK), and Wheeler (WH) areas. The locations of the three lines are marked with yellow arrows in Figure 3-18. The temperature probes were installed at depths 0.70 to

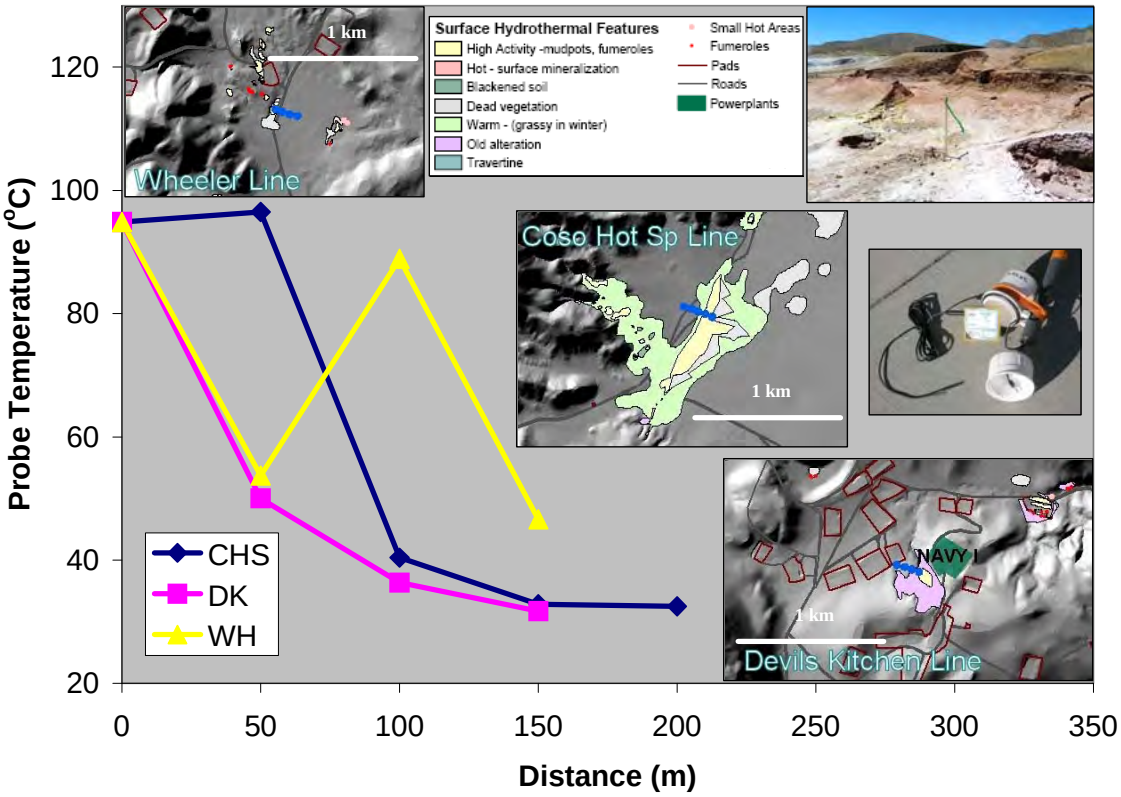

Figure 3-18. Subsurface temperatures measured at 13 locations (blue circles in map insets) across hydrothermal features, as indicated: CHS – Coso Hot Springs, DK – Devel's Kitchen, and WH – Wheeler. Distance is measured from the first probe along each line, starting within features and moving outwards. Photo insets show a probe and the surroundings of the CHS-2 probe. Map insets, courtesy of Bethiah Hall, formerly at the US Navy Geothermal Program Office (China Lake, CA). Steve Bjornstad from GPO was in charge of the installation of and data collection from the temperature probes.

Photo Credit: Steve Bjornstad, GPO (two insets in upper right)

0.90 m, as rock permitted, 50 m apart for each line. The recordings lasted about a week during which subsurface temperatures remained constant for any given site. As could be expected, in each of the three groups, the temperatures decrease in the direction from the center of a hydrothermal feature towards its periphery.

The surface temperature was also measured with a rented hand-held infrared camera FLIR P65, at the time of the satellite passage, around noon during the day and 11 pm during the night. This was mostly done at distances 2 to 3 m from the locations where the temperature probes were installed, as well as from a distance towards the surrounding rhyolite domes and hills. Although the FLIR images could not be compared with the cloudy ASTER data collected at the same time, they are rather unique and it is instructional to examine the small-scale spatial distribution of surface temperature (Figures 3-19 and 3-20).

Although the AST_08 and AST_07XT products incorporate a standard atmospheric correction, a better correction may be achieved if specific profiles of atmospheric temperature, water vapor, and pressure are available at the time of overflight of the satellite. For this reason,

such data were collected by launching radiosondes about half an hour before the two satellite passages, during the day, and at night. This was done with the assistance of the ASTER team at the Jet Propulsion Laboratory (JPL).

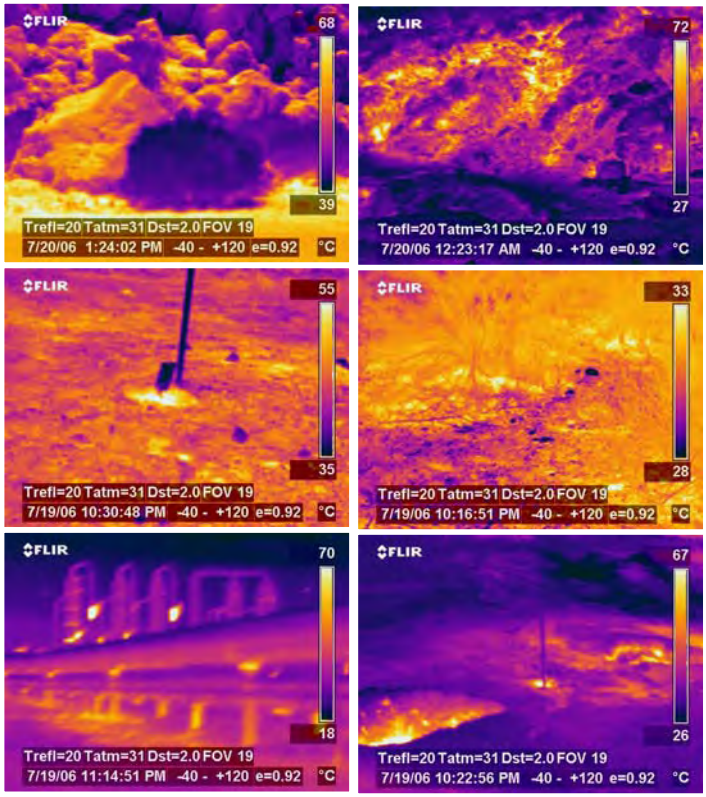

Figure 3-19. Thermal images taken in the field during the night with a FLIR-P65 infrared camera. Color bars show temperature in °C. Clockwise from upper left,: a bush in front of rocks, one of the known hot areas, dry brush and gravel, mud bubbles at the Coso Hot Springs area, electricity producing plant, and location of one of the temperature probes (see hotter surface where the probe is stuck in the ground).

Photo Credit: Mariana Eneva, Imageair Inc.

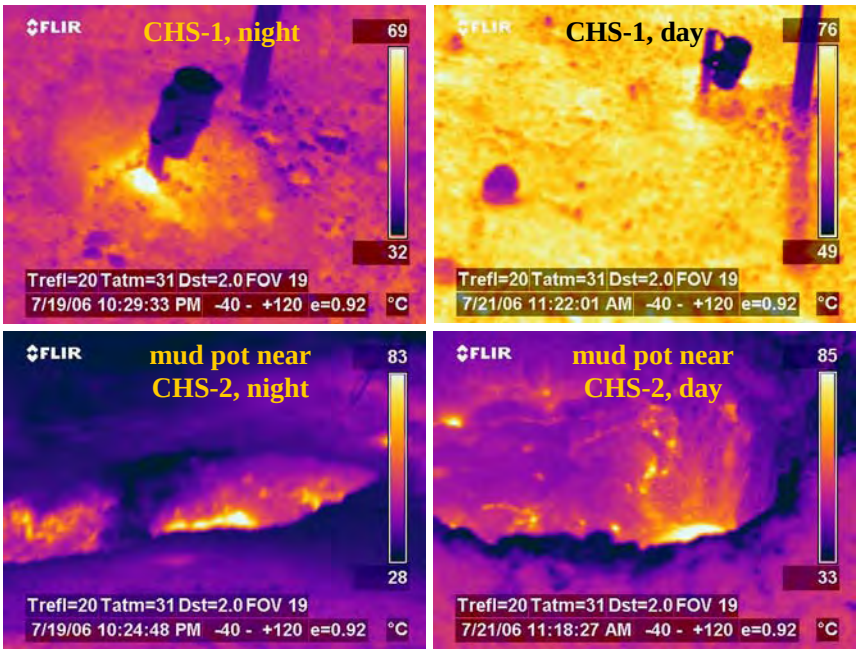

Figure 3-20. Surface temperature measured with a hand-held FLIR-P65 infrared camera close to the times of satellite passages. Left – nighttime images; right – daytime images. Top – vicinity of the CHS-1 probe. Note that probe and demarcation pole are cooler, while surface around probe is hotter due to ground disturbance. Bottom – mud pots near the CHS-2 probe. CHS – Coso Hot Springs. Color bars show temperature in °C.

Photo Credit: Mariana Eneva, Imageair Inc.

Figure 3-21. Launching a radiosonde for atmospheric measurements.
Photo Credit: Mariana Eneva, Imageair Inc.

3.5.2. August 2006

Since the ASTER images collected in July 2006 were very cloudy, another field trip took place in August 2006. This time clear ASTER images were collected, both during the day and at night (Figure 3-22). Due to expense and logistic difficulties, radiosondes were not re-launched, and neither was a thermal infrared camera used.

A hand-held ASD FieldSpec spectroradiometer, borrowed from the Department of Geography, San Diego State University (SDSU), was used to measure the reflectance of contrasting surfaces such as bare soil, volcanic rock, red cinder, gravel, dirt road, and dry and live sage bush. Even though the spectroradiometer was available during the July 2006 trip as well, it could not be utilized in the presence of clouds. The purpose in August 2006 was to collect reflectance data in order to correct the AST_08 images for albedo. Reflectance measurements were collected at 15 locations over surfaces of different color and texture, around the time of daytime satellite passage. The locations of reflectance measurements are marked in Figure 3-22 with green arrows. Examples of reflectance spectra are shown in Figure 3-23. These field data were used to evaluate the k_w and b_w coefficients in eq. 2 (Section 2.2.4) in the relationship between the spaceborne reflectance data (AST_07XT) and the product of albedo and topographic slopes (Coolbaugh et al. 2007a). It was estimated that k_w is between 0.50 and 0.55 and b_w between 0.11 and 0.16 for the three VNIR bands (Figure 3-24).

In addition, an Omega OS534E infrared thermometer was installed in the area of the Coso Wash, pointed at bare soil and logging data over a two day period. Figure 3-22 shows its location (pink arrow) and Figure 3-25 shows the recorded surface temperatures, as well as images of the thermometer installation. The diurnal change of observed temperature was used to estimate coefficients for the combination of daytime and nighttime AST_08 in order to remove the effect of thermal inertia. These coefficients were in agreement with the ones

determined from the minimum variance when combining the two images (nighttime/ day-time ratio ~0.6/0.4).

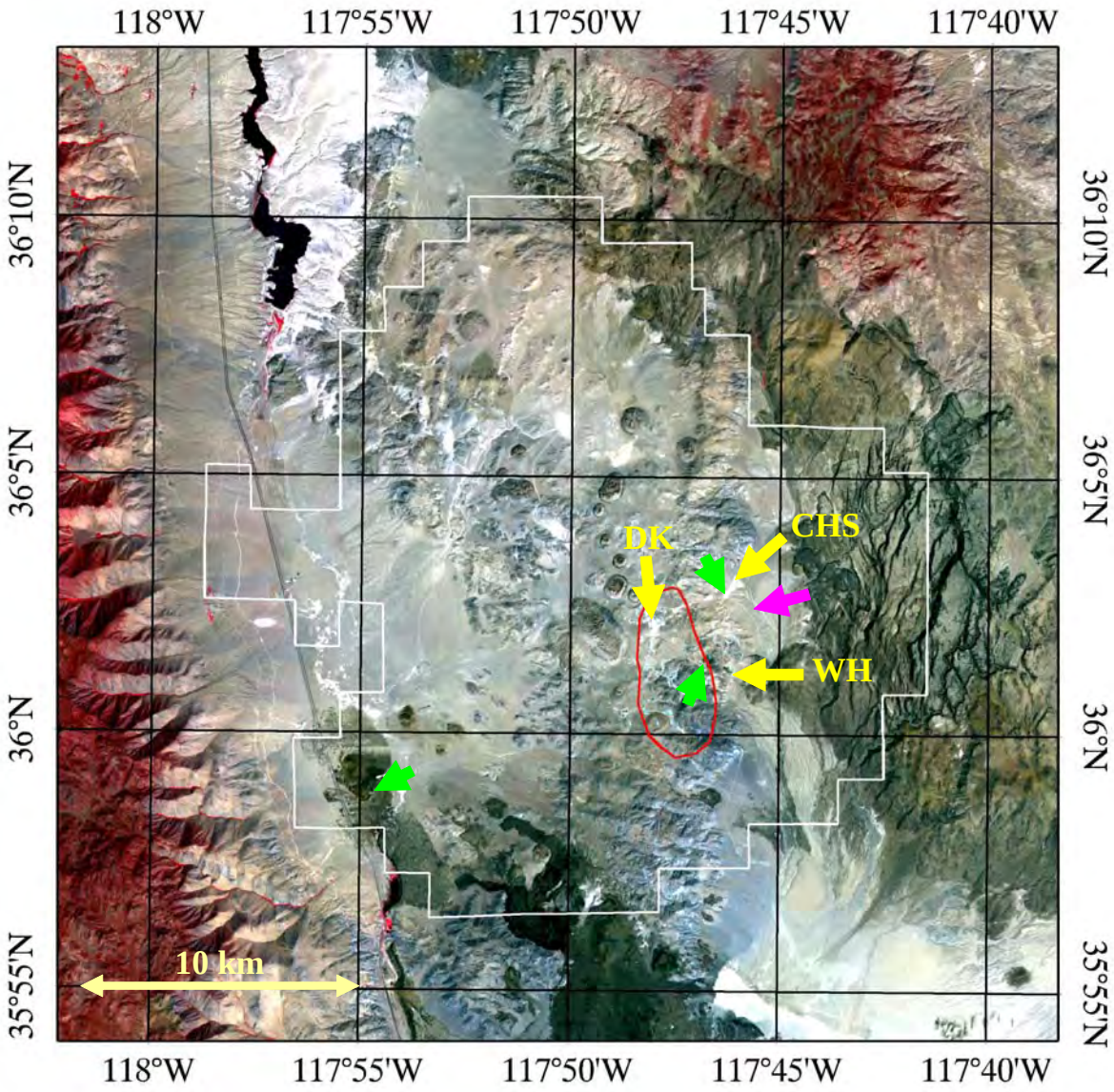

Figure 3-22. ASTER coverage of the Coso KGRA (white polygon) extracted from two Level 1B VNIR images collected at 11:45 am (local daylight savings time) on August 22, 2006 (RGB: R=band 3, G=band 2, B=band 1). Production area is shown with a red outline. Yellow arrows point to locations of temperature probes along three lines in the Coso Hot Springs (CHS), Devil's Kitchen (DK), and Wheeler (WH) areas. Green arrows show locations of reflectance measurements. Magenta arrow points to the location where an infrared thermometer was installed.

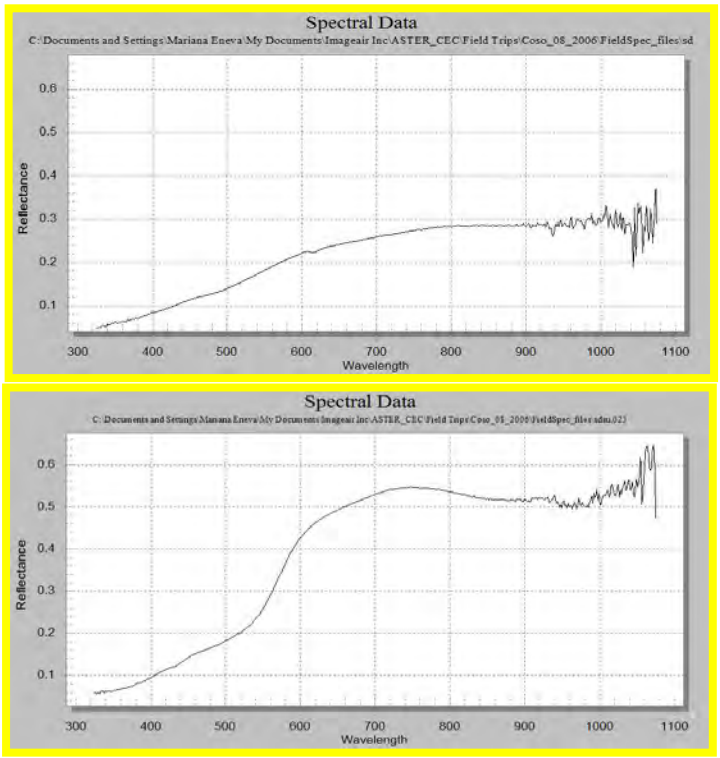

Figure 3-23. Examples of reflection spectra collected in the field with an ASD FieldSpec spectroradiometer. Light-colored surfaces give off more reflection, hence the albedo is higher.

Photo Credit: Mariana Eneva, Imageair Inc.

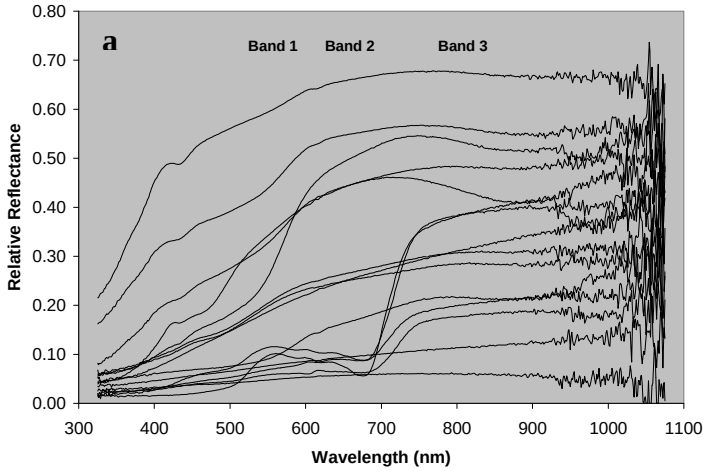

Figure 3-24. Reflectance measured at various locations with a hand-held ASD FieldSpec spectroradiometer. Wavebands 1 to 3 correspond to ASTER VNIR. (a) Individual reflectance curves at various locations. Dark to light surfaces are represented by increasing reflectance. (b) ASTER reflectance versus product of shaded relief (related to topographic slope) and albedo measured in the field. Fitted straight lines are used to estimate coefficients as described in the text.

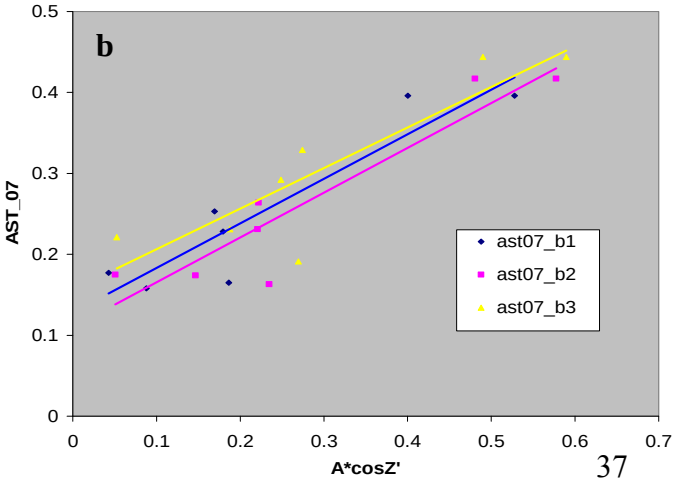

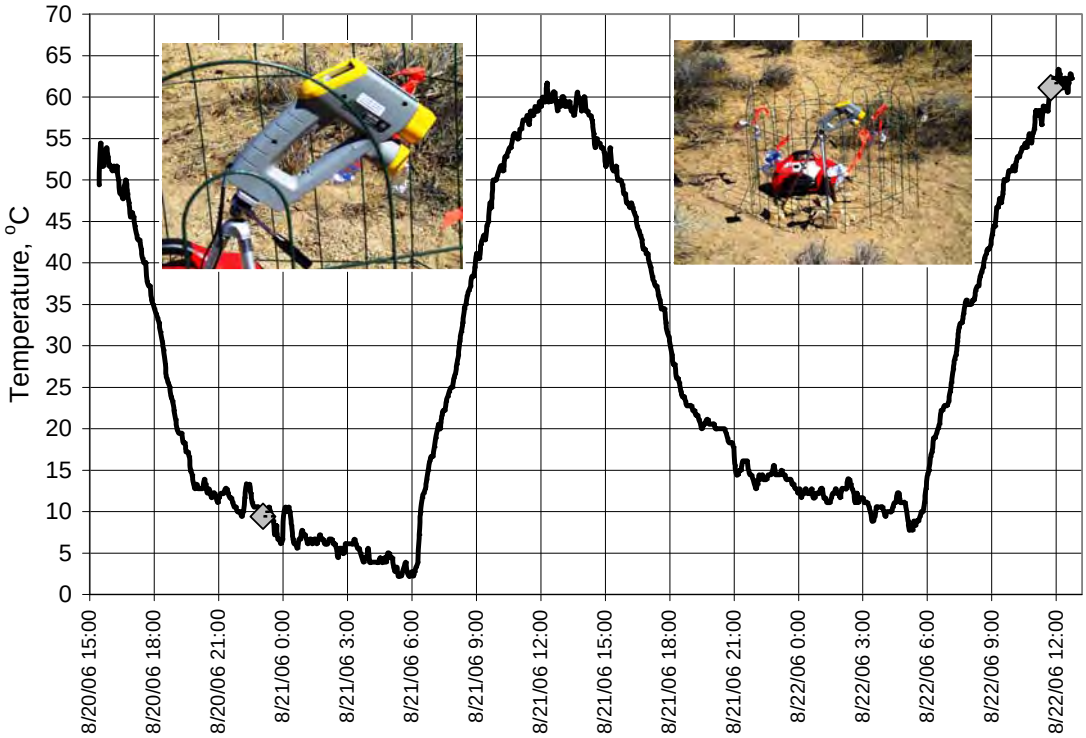

Figure 3-25. Surface temperature measurements with an infrared thermometer over two days in August 2006. Grey diamonds indicate temperatures at the times of satellite passage. Insets show thermometer installation, with a portable power supply and a fence and ribbons to deter burros.

Photo Credit: Mariana Eneva, Imageair Inc.

3.5.3. May and June 2009

Shallow temperature surveys (Figure 3-26) were conducted in eight different valleys in eastern California (Figure 3-27). The equipment and techniques used to make two-meter-deep temperature measurements are discussed in detail by Coolbaugh et al. (2007b) and Sladek et al. (2007). Kratt et al. (2008, 2009) discussed at least four hidden geothermal systems that were discovered with this method as a result of previous surveys.

The methodology involves the use of an All-Terrain Vehicle (ATV) to transport a generator and all equipment (Fig. 3-26). A demolition hammer is used to drive a ~5/8" wide, tungsten-carbide-steel-tipped hollow rod into the ground, Resistance Temperature Devices (RTDs) are inserted into each rod, and after at least a one-hour equilibration time the temperature is recorded. During the initial part of such a survey, measurements are made at approximately 1 km intervals, and if temperature anomalies are found, additional measurements are taken with closer spacing.

Due to the ease of travel and possible land use regulations, it is preferable to use existing roads that generally parallel a range-front or transect other structurally favorable areas. Such roads typically traverse alluvial fans or lacustrine deposits that are more easily penetrated with the hammer and rods.

Figure 3-26. Deployment of 2-m temperature probes. Operators Chris Kratt (on top of ATV) from the Desert Research Institute and Mark Coolbaugh from the University of Nevada Reno.

Photo Credit: Mariana Eneva, Imageair Inc.

Over 160 measurements were made, covering a total distance of over 160 km. Figure 3-28 shows the 2-m temperature data for each of the eight valleys. During this type of surveys, variations in local background temperatures are often encountered, as temperatures vary

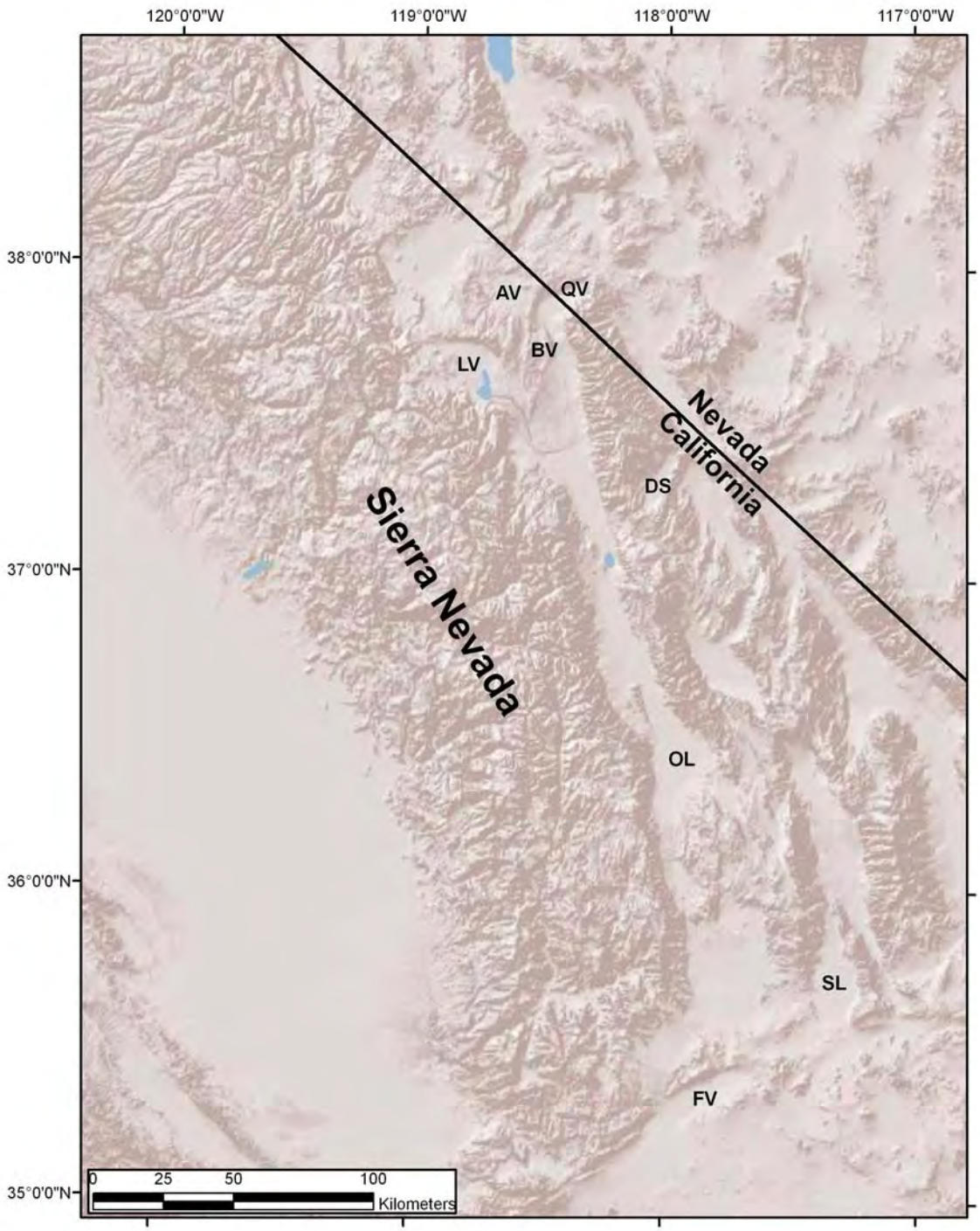

Figure 3-27. Shaded relief image showing location of areas where 2-m temperature probes were deployed. AV - Adobe Valley, LV - Long Valley, BV - Benton Valley, QV - Queen Valley, DS - Deep Springs Valley, OL - Owens Lake, SL - Searles Lake, FV - Fremont Valley.

both with season and latitude. Several other factors also create inter- and intra-valley variability among background measurements. For example, shallow depths to groundwater and increased soil moisture cause background temperatures to be lower, unless they are measured in a distinct thermal zone. In addition, albedo (i.e., the darkness or brightness of a surface), can also cause shallow temperatures to be warmer under darker surfaces and cooler

under lighter-colored ones. Finally, differences in the thermal inertia of various geologic units can also influence 2-m temperatures. These factors are the same as the ones discussed in connection to the satellite TIR imagery (Section 2.2). Thus a large portion of the variability among the data in such surveys can be explained by these factors. The task is to evaluate if there are variations that go beyond such artifacts, possibly connected with geothermal systems.

Data from basins with similar latitudes and elevations were sometimes examined collectively in order to ascertain background temperatures. Otherwise, data from each valley were analyzed separately for thermal anomalies. In previous work (Kratt et al. 2008, 2009), thermal anomalies were recognized in part by a pattern of temperature observations that cool off in all directions from the location of a central peak temperature (e.g., Figure 3-29). Here, the southeast corner of Owens Lake Valley was the only survey location with a temperature pattern potentially characteristic of a possible geothermal system. The temperatures steadily increase from about 19° C in a northeasterly direction to a peak of 23.6^{o} C, after which they begin to steadily cool down as the transect parallels the range-front to the northeast. However, when 2-m temperatures for the Owens Lake Valley survey are plotted against ground albedos estimated from daytime AST_07XT imagery (Figure 3-30), it becomes apparent that the higher temperatures in the southeast corner of the valley are likely attributable to greater absorption of solar radiation (i.e. darker surfaces), and not due to geothermal heat flux.

For several of the other surveys, including those at Fremont Valley and Deep Springs Valley, 2-m temperatures decrease as the survey lines approach playas or areas with shallow groundwater. This is especially evident in Fremont Valley, where temperatures below the background albedo-temperature line mark areas of shallow groundwater and/or higher soil moisture content at the valley bottom near irrigated fields (Figure 3-31). Such temperature anomalies are easily distinguished from geothermal heat flux anomalies, which in contrast, show above the background temperature-albedo line (Figure 3-32), as exemplified by Columbus Marsh in Nevada (Kratt et al. 2009, Sladek et al. 2009).

Thus the 2-m temperature surveys did not reveal any obvious areas of possible geothermal resources. This does not preclude that geothermal resources with surface temperature expression may exist elsewhere in the region.

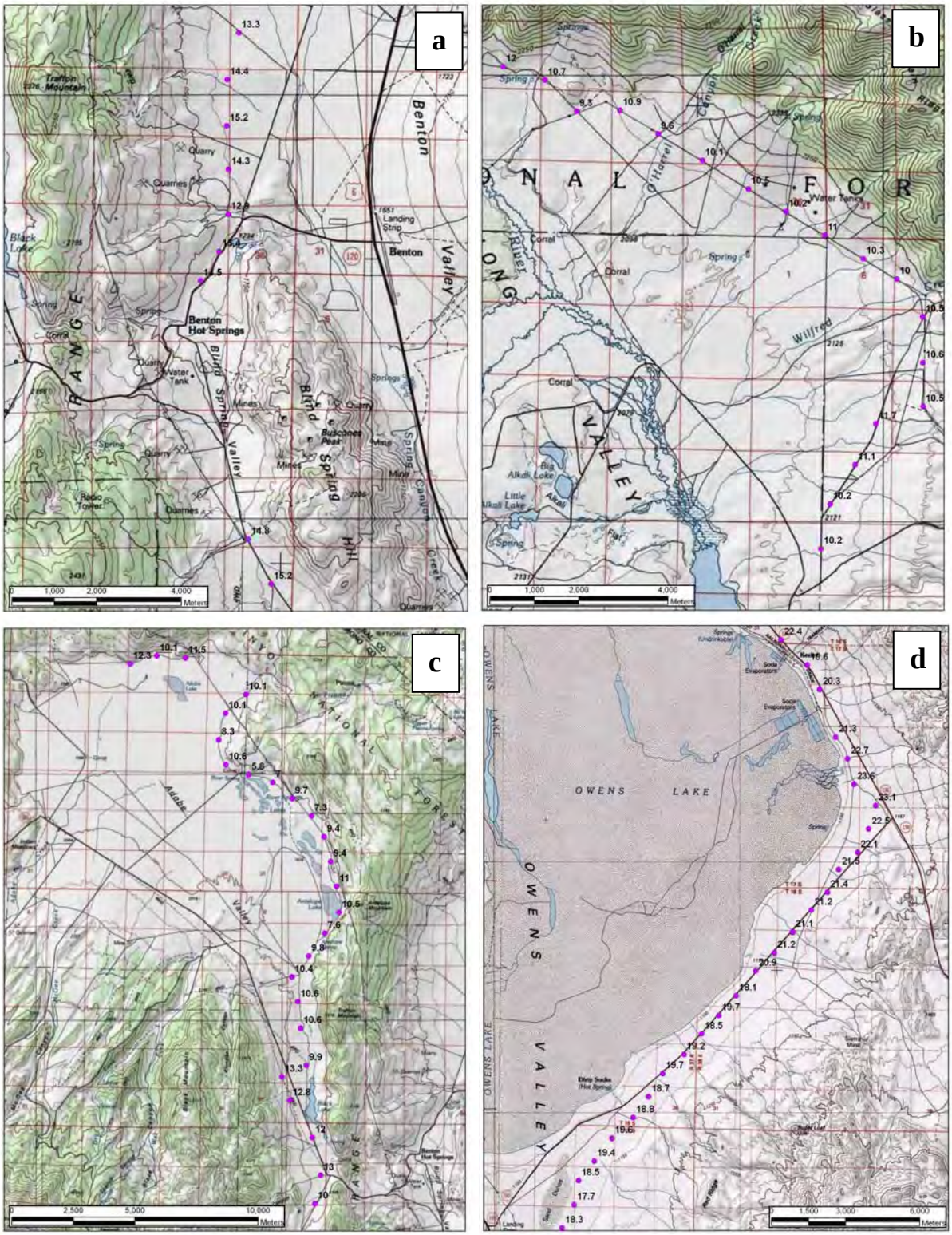

Figure 3-28. Measurements of 2-m temperatures. Locations are marked with pink circles. The temperatures in ^{o}C are marked next to the circles. (a) Benton Valley. (b) Long Valley. (c) Adobe Valley. (d) Owens Lake Valley.

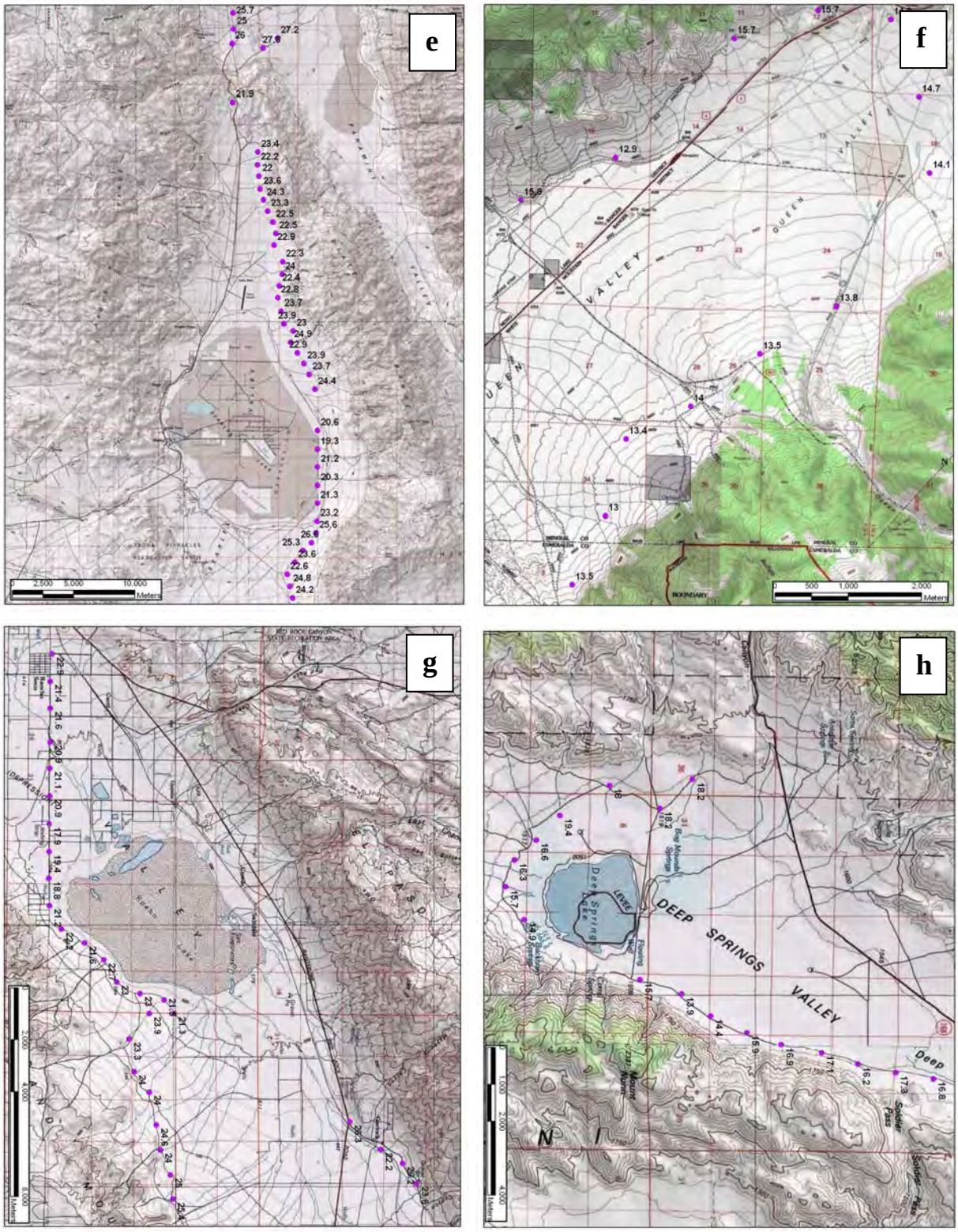

Figure 3-28 continued. (e) Searles Lake Valley. (f) Queen Valley. (g) Fremont Valley. (h) Deep Springs Valley.

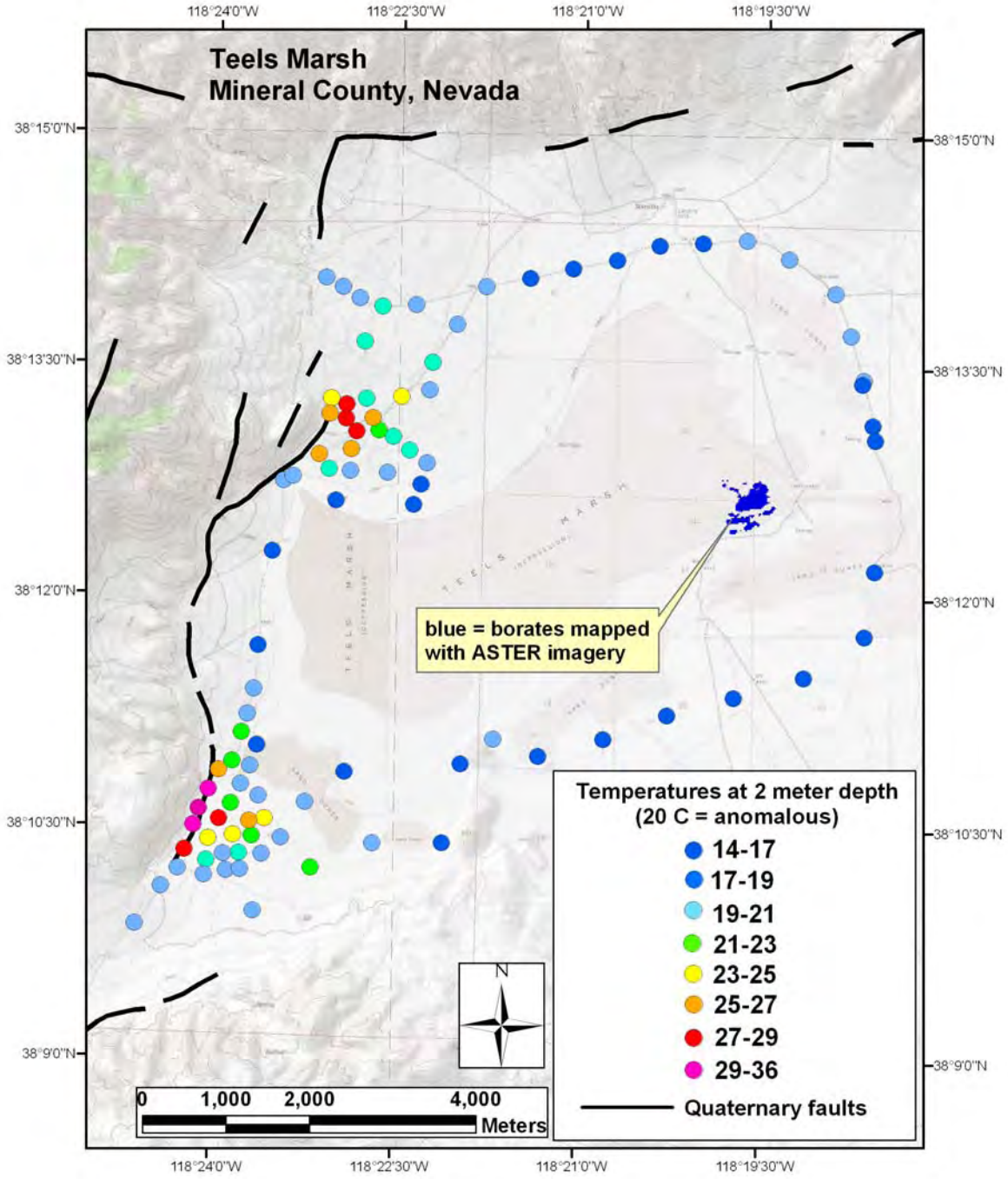

Figure 3-29. Example of a pattern of shallow temperature measurements delineating a geothermal anomaly.

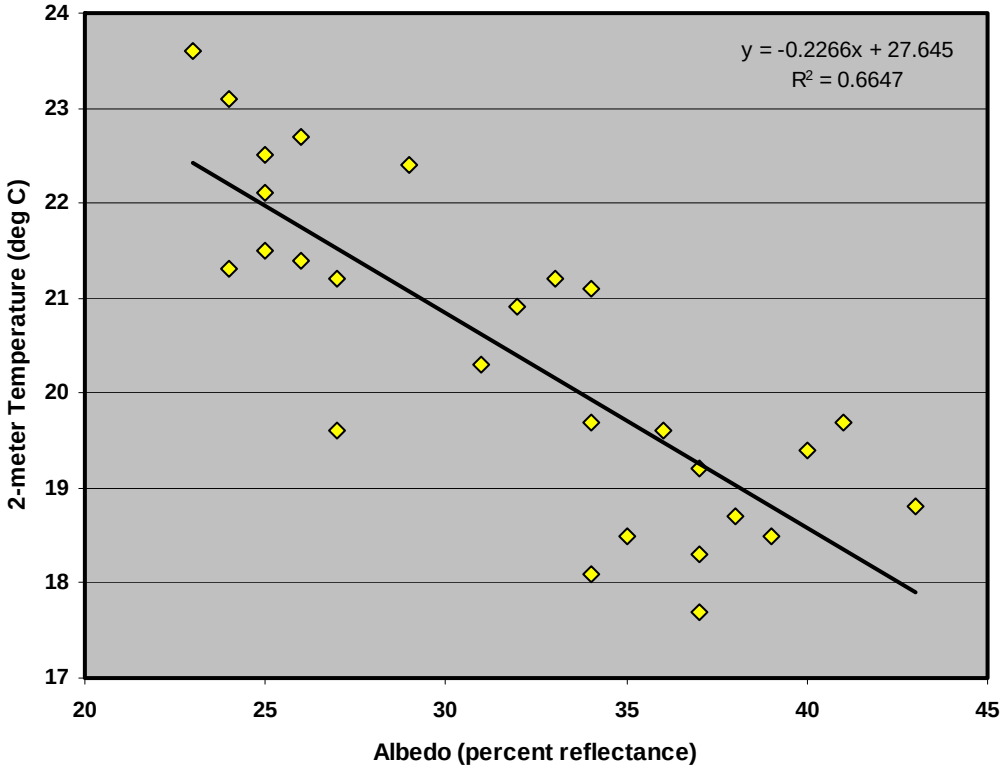

Figure 3-30. Example from Owens Valley, where lower albedo causes greater absorption of solar energy and therefore warmer 2-meter background temperatures.

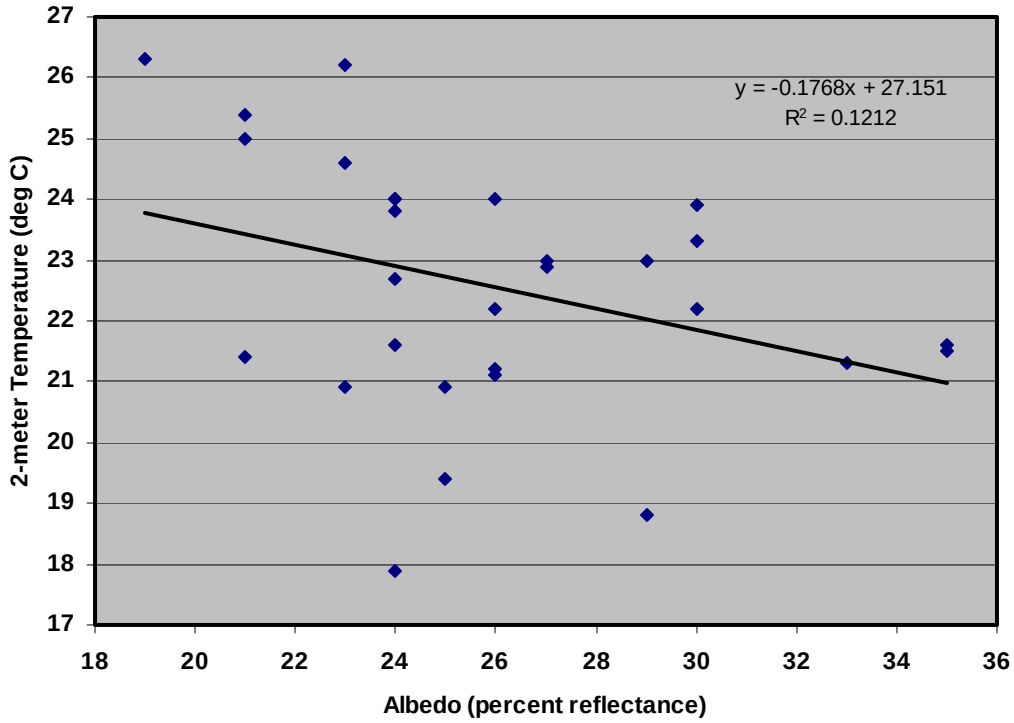

Figure 3-31. Example from Fremont Valley, where data significantly below the albedo-temperature background line are associated with shallow groundwater in the valley bottom near irrigated fields.

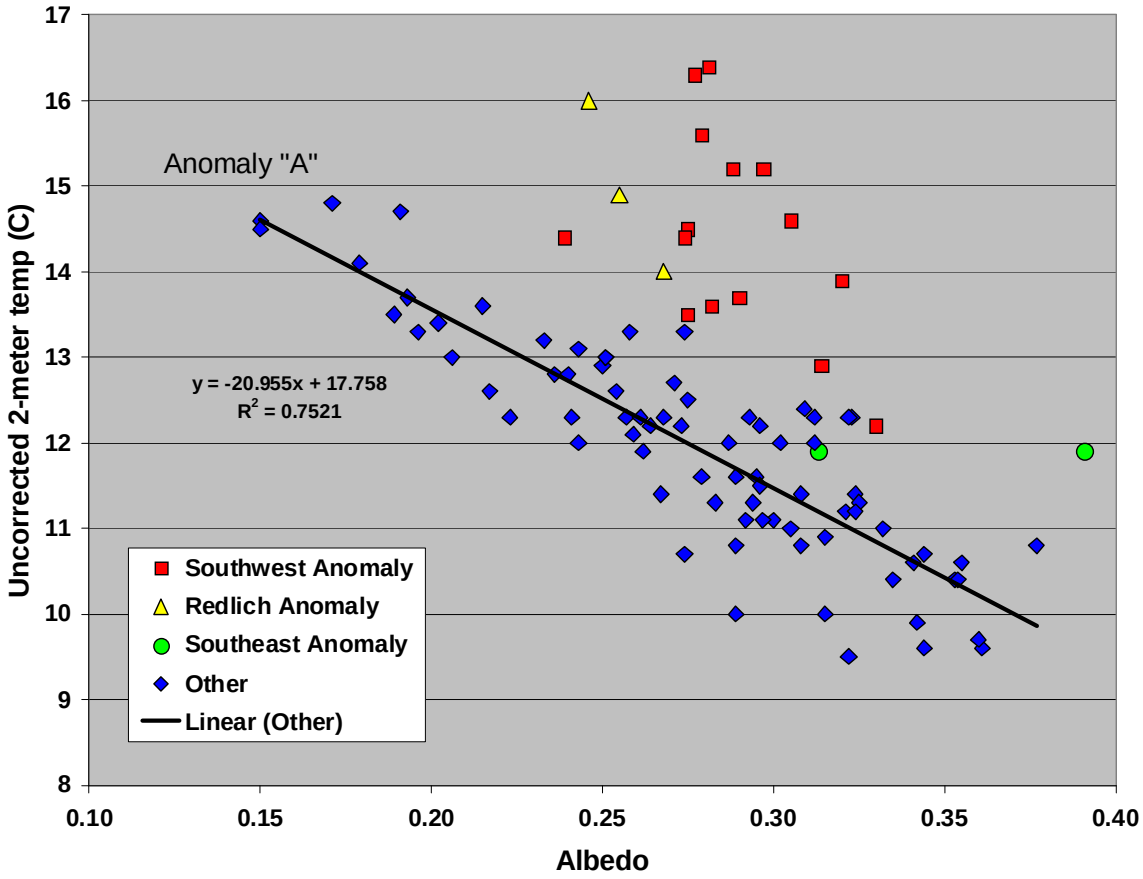

Figure 3-32. 2-meter temperatures and associated albedos from the Columbus Marsh playa, Nevada. Temperature data are from Kratt et al. (2009). Albedos were taken from band 2 of an atmospherically corrected AST_07XT satellite image. Albedos from the image at selected locations were compared to equivalent values measured in the field with a spectrometer to ensure that the image data were scaled properly to represent albedo. Topographic slope aspects were near horizontal in all parts of the survey.

4.0 Conclusions and Recommendations

Satellite thermal infrared (TIR) imagery can be potentially very useful as a cost-effective tool to search for geothermal resources associated with increased surface temperatures. However, adequate interpretation for the purpose of exploration is only possible if the TIR imagery is corrected for several effects unrelated to geothermal characteristics. Ground-based field measurements can significantly contribute to complement the results of remote sensing.

It is recommended that future studies first focus on resolving the current inadequacy of orthorecification methods needed to remove the terrain distortions in the thermal infrared (TIR) imagery. It will be important to assure easily accessible orthroectifcation techniques that can successfully work with the satellite TIR products from ASTER and successor satellite sensors. This will make it possible to efficiently study large areas with significant topographic variability.

After temperature anomalies are unambiguously identified in known geothermal areas, it is further recommended to look for similar markers in other areas that may be prospective future sites of geothermal production.

Furthermore, it will be important to assure in the future a more complete utilization of the available remote sensing data and capabilities, by augmenting the satellite TIR studies with a search for mineral alteration associated with geothermal resources. This is necessary, because not all geothermal resources are associated with elevated surface temperatures.

The immediate benefit to California is that this study has started the search for temperature anomalies in a prospective region of geothermal resources. Most possible pitfalls have been identified and a methodology has been established to distinguish between real and irrelevant temperature anomalies in satellite TIR imagery. This would significantly facilitate future exploration studies of this type.

As a longer-term benefit to California, such methods, in conjunction with other applications of remote sensing, will contribute to the future discovery of new geothermal resources. This is important in view of the planned increase of renewable energy used for electricity generation and related creation of more jobs in California.

5.0 References

Allis, R.G., G.D. Nash, and S.D. Johnson, 1999. "Conversion of thermal infrared surveys to heat flow: Comparison from Dixie Valley, Nevada, and Wairakei, New Zealand." *Geothermal Resources Council Transactions*, v. 23, p. 499-504.

Calvin, W., M. Coolbaugh, and R.G. Vaughan, 2002. "Geothermal site characterization using multi- and hyperspectral imagery." *Geothermal Resources Council Transactions*, v. 26, p. 483-484.

Chapman, L., J.E. Thornes, and A.V. Bradley, 2001. "Statistical modeling of road surface temperature from a geographical parameter database," *Meteorological Applications*, v. 8, p. 409-419.

Cochrane, G.R., M.A. Mongillo, P.R.L. Browne, and J.P. Deroin, 1994. "Satellite studies of the Waimangu and Waiotapu geothermal areas, TVZ." In *Proceed. 16th NZ Geothermal Workshop*, p. 181-198.

Coolbaugh, M.F., 2003. *The Prediction and Detection of Geothermal Systems at Regional and Local Scales in Nevada Using a Geographic Information System, Spatial Statistics, and Thermal Infrared Imagery.* Ph.D. Thesis, University of Nevada Reno.

Coolbaugh, M.F., J.V. Taranik, and F.A. Kruse, 2000. "Mapping of surface geothermal anomalies at Steamboat Springs, NV using NASA Thermal Infrared Imaging Spectrometer (TIMS) and Advanced Visible and Infrared Imaging Spectrometer (AVIRIS) data." In *Proceed. 14th Thematic Conf. Appl. Geologic Remote Sensing, Ann Arbor, MI*, p. 623-630.

Coolbaugh, M.F., C. Kratt, A. Fallacaro, W.M. Calvin, and J.V. Taranik, 2007a. "Detection of geothermal anomalies using Advanced Spaceborne Thermal Emission and Reflection Radiometer (ASTER) thermal infrared images at Brady's Hot Springs, Nevada, USA," *Remote Sensing of Environment*, . v. 106, p. 350-359.

Coolbaugh, M.F., C. Sladek, J.E. Faulds, R.E. Zehner, and G.L. Oppliger, 2007b. "Use of rapid temperature measurements at a 2-meter depth to augment deeper temperature gradient drilling." In *Proceedings, 32nd Workshop on Geothermal Reservoir Engineering, Stanford University, Stanford, CA, Jan. 22-24, 2007*, p. 109-116.

Crippen, R., and R. Blom, 2001. "Unveiling the lithology of vegetated terrains in remotely sensed imagery." *Photogr. Eng. Rem. Sens*., p. 935-944.

Eneva, M., M.F. Coolbaugh, and J. Combs, 2006. "Application of satellite thermal infrared imagery to geothermal exploration in east central California," *Geothermal Resources Council Transactions*, v. 30, p. 407-411.

Eneva, M., M. Coolbaugh, S. Bjornstad, and J. Combs, 2007. "Detection of surface temperature anomalies in the Coso geothermal field using thermal infrared remote sensing," *Geothermal Resources Council Transactions*, v.31, p. 335-340.

Eneva, M., and M. Coolbaugh, 2009. Importance of elevation and temperature inversions for the interpretation of thermal infrared satellite images used in geothermal exploration," *Geothermal Resources Council Transactions* v. 33, p. 467-470.

Finlayson-Pitts, B.J., and J.N. Pitts, Jr., 1999. *Chemistry of the upper and lower atmosphere: Theory, experiments, and applications.* Academic Press, pp. 969.

Gillespie, A.R., S. Rokugawa, T. Matsunaga, J.S. Cothern, S. Hook, and A.B. Kahle, 1998. "A temperature and emissivity separation algorithm for Advanced Spaceborne Thermal Emission and Reflection Radiometer (ASTER) images," *IEEE Transactions on Geoscience and Remote Sensing*, v. 36, p. 1113-1126.

Kratt, C., M.F. Coolbaugh, and W.M. Calvin (2006). "Remote detection of Quaternary borate deposits with ASTER satellite imagery as a geothermal exploration tool," *Geothermal Resources Council Transactions*, v. 30, p. 435-439.

Kratt, C., M. Coolbaugh, C. Sladek, R. Zehner, R. Penfield, and B. Delwiche, 2008. "A new gold pan for the west: Discovering blind geothermal systems with shallow temperature surveys." *Geothermal Resources Council Transactions*, v. 32, p. 153-158.

Kratt, C., M.F. Coolbaugh, B. Peppin, and C. Sladek, 2009. "Identification of a new blind geothermal system with hyperspectral remote sensing and shallow temperature measurements at Columbus Salt Marsh, Esmeralda County, Nevada." *Geothermal Resources Council Transactions*, v. 33, p. 481-486.

Martini, B.A., E.A. Silver, D.C. Potts, and W.L. Pickles, 2000. "Geological and geobotanical studies of Long Valley Caldera, CA, USA utilizing new 5-m hyperspectral imagery." In *Proceed. IEEE Int. Geoscience Remote Sensing Symposium, July 2000*.

Monastero, F.C., 2002. "Model for success: An overview of industry-military cooperation in the development of power operations at the Coso Geothermal Field in southern California." *Geothermal Resources Council Bulletin*, p. 188-194.

Pickles, W.L., P.W. Kasameyer, B.A. Martini, D.C. Potts, and E.A. Silver, 2001. "Geobotanical remote sensing for geothermal exploration." *Geothermal Resources Council Transactions*, v. 25, p. 307-312.

Quattrochi, D.A., A. Prakash, M. Eneva, R. Wright, D.K. Hall, M. Anderson, W.P.Kustas, R.G. Allen, T. Pagano, M.F. Coolbaugh, 2009. "Thermal remote sensing: Theory, sensors, and applications," Chapter 3, In *Manual of Remote Sensing*, American Society of Photogrammetry and Remote Sensing, Fall Church, VA, p. 107-187.

Sass, J., and S. Priest, 2002. "Geothermal California: California claims the world's highest geothermal power output, with potential for even more production with advanced techniques." *Geothermal Resources Council Bulletin*, p. 183-187.

Sladek, C., M.F. Coolbaugh, and R.E. Zehner, 2007. "Development of 2-meter soil temperature probes and results of temperature survey conducted at Desert Peak, Nevada, USA." *Geothermal Resources Council Transactions*, v. 31, p. 363-368.

Sladek, C., M.F. Coolbaugh, and C. Kratt, 2009. "Improvements in shallow (2-meter) temperature measurements and data interpretation." *Geothermal Resources Council Transactions*, v. 33, p. 535-542.

Tonooka, H., 2001. "An atmospheric correction algorithm for thermal infrared multispectral data over land—A water-vapor scaling method." *IEEE Transactions Geoscience Remote Sensing*, v. 39, p. 682-692.

Watson, K., 1973. "Periodic heating of a layer over a semi-infinite solid." *J. Geophys. Res.*, v. 78, p. 5904-5910.

Williams, C.F., 2002. "Geothermal systems of the Great Basin and U.S. Geological Survey plans for a regional resource assessment." *Geothermal Resources Council Transactions*, v. 26, p. 547-550.

Wu, X., 2008. "A simplified orthorectification approach for satellite imagery," *The International Archives of the Photogrammetry, Remote Sensing and Spatial Information Sciences*, v. XXXVII - Part B3a. Beijing.